

Fig. 15: Schematics of material transfer and key deformation features in the model domain. Section parallel to shortening of direction (a) shows thrusting of oroclinal hinge, upright folding and side flow of lower lithosphere, while (b) show deformation and material redistribution between both oroclinal limbs (b1) and asymmetrical folding of basal layers and forming of the pop up/down structures as product of mechanical coupling between ductile lower and brittle upper crust (b2) (*modified after Krýza et al. 2019*).

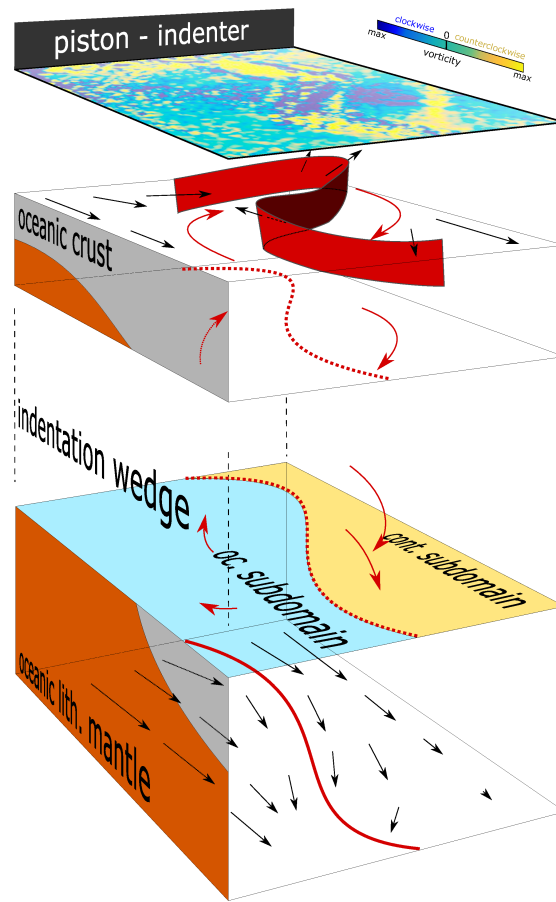


Fig. 16: The blockdiagram of the model inner dynamics. At the top is shown the contour map of the vorticity that reveals a clockwise rotation of the orocline inflection and counterclockwise rotation of the orocline outer limbs. The black arrows correspond to material flow from indenter side to backstop while red arrows show a decreasing vorticity in a material transfer from surface to basement. The red curve represents an interface between oceanic and continental subdomains.

#### 2.5.4 Why the O→C and C→O hinges have opposite inclinations?

Fig. 15a and Fig. 16 show thrusting of oceanic over continental lithosphere in the O→C fold hinge and continental over oceanic in the C→O fold hinge. This requires that the O→C fold hinge plunges towards the oceanic subdomain and that the C→O fold hinge plunges towards the continental subdomain. The inclination angle of fold axes and associated thrusts of the lithospheric segments is governed by difference in vortex velocity between the mantle and upper crust as deduced from the serial sections and the PIV analysis of the surface deformation (Fig. 11, 12, 13, 16). It can be shown that the vortex velocity at the surface is high compared to slower flow of the viscous mantle at depth (Fig. 16). This velocity difference implies a progressive rotation of the fold axes from vertical to less inclined positions and the above described thrusting of mantle lithosphere.

### 2.5.5 Is the deformation driven by top or bottom fluxes?

Tikoff and Teyssier (2002) discuss the deformation of the lithosphere and argue that it occurs either by the movements of mantle layer (i.e. bottom driven tectonics) or by the rigid crust (i.e. top driven tectonics). In order to determine which of these two models is the more likely, it is necessary to determine which layer is mechanically dominant and controls deformation of the whole system. We have shown that the primary response of the mantle lithosphere with a low mechanical anisotropy is the development of a typical indentation profile (Fig. 12 and Fig. 13 – lateral view; Figure 14a – velocity field) and this has been simulated numerically by England and Houseman (1989). Both crustal sections and surface analysis show that during the early stages of the experiments the mantle governs the bulk lithospheric deformation. However, this behavior changes rapidly after ca. 5-10% shortening i.e. during the maximum amplification of the O→C and C→O folds within crust. The significant crustal flow related to fold amplification affects the mantle flow, so the originally developed indentation profile is modified by lateral redistribution of the continental and oceanic mantle. During this stage, it is the folding of the accretionary belt that governs bulk material fluxes in its vicinity leading to the accumulation of oceanic mantle material in the O→C fold and of continental crustal material in the C→O fold. After ca. 30% shortening the active folding ceases and post-buckle flattening i.e. homogeneous flattening takes over. The deformation becomes partitioning between the O→C and C→O folds because of the different integrated strengths of these two domains. During this stage the lithospheric deformation progressively passes to mechanically coupled behavior.

### 2.5.6 Implications for geodynamic concepts of curved orogenic belts

Both continental and oceanic lithospheres possess a horizontal stratification characterized by strong upper crust and upper mantle layers. This distribution of rheologically contrasting layers is responsible for typical deformation of the lithosphere such as the formation of thrust and fold belts, continental indentation or “crocodile” type wedging (Burg et al., 1998; Midtkandal et al., 2013). In contrast, oroclines are governed by the presence of vertical strong layer that fold around vertical axis (Pastor-Galán et al., 2012). The primary prerequisite for oroclinal buckling is the existence of a competent and vertical layer surrounded by less competent material. The most common mechanism bringing strong lithosphere into a vertical position is subduction of an oceanic plate as has occurred for example along the western Pacific margin. Here, the vertical subduction and accretionary system separates the back arc region formed by stretched continental crust, marginal basins and arcs from old oceanic lithosphere. These two systems are characterized by horizontal stratification and highly contrasting bulk rheology. There are several examples along the western Pacific margin showing high curvature of a subduction system interpreted as a result

of passive oroclinal bending related to differential subduction retreat (Menant et al., 2016; Rosenbaum and Lister, 2004).

The model presented in this work shows the behavior of such a system when it is compressed parallel to the subduction zone. Such systems are well known from Central Asia, where the giant Paleozoic Kazakh and Mongolian oroclines occur (Şengör et al., 1993; Şengör and Natal'In, 1996; Yakubchuk, 2005). The well-studied Mongolian orocline is formed by a folded subduction system surrounded by horizontally stratified pericontinental complexes and relaminated oceanic domains called here CAW (e.g. Edel et al., 2014; Lehmann et al., 2010). In this region the C→O and O→C systems exist and their deformation can be explained in the light of model predictions presented above.

The gravity data show large-scale redistribution of the lower crust (Guy et al., 2015) and the development of magmatic provinces spatially related to the orocline geometry (Guy et al., 2014b). In particular, it is a major gravity low in the hinge area of the Mongolian orocline, along its axial plane more or less coinciding with the Permian Hangay and Triassic Khentey alkaline plutonic provinces (Fig. 17a). This alkaline intraplate magmatism was previously interpreted as a result of migration of South Khangai hot spot (e.g. Kovalenko et al., 2004; Yarmolyuk et al., 2007) but may be a proxy of giant elevation of hot lower crust and thermally perturbed mantle in the hinge zone and axial plane of the orocline as predicted by our model. In our model, the elevation of hot mantle (Fig. 11 and 17 – oceanic subdomain fold) might result in its melting and development of massive alkaline magmatic provinces in the region. The presence of hot and low viscosity felsic material at depths that is depicted in the whole accretionary system of southern Mongolia as a source of magmatism (Guy et al., 2014a; 2015; Nguyen et al., 2018) is a necessary requirement to accommodate deformation in both hinge and limb areas of orocline. Petrological and geophysical studies show linear belts of Permian granulites associated with important narrow gravity and magnetic lineaments (Fig. 17b and c) that coincide with extrusions of this exceptionally hot granulitic crust along orocline hinge and limb areas in the Chinese Altai (Li et al., 2004; Broussolle et al., 2018a; 2019). Similarly, E-W trending deformation zones associated to alkaline magmatism coinciding with magnetic lineaments and vertical deformation zones (Seltmann et al., 2011; Guy et al., 2014b) were reported from the study region (Fig. 17c). These recent observations indicate a major mobility of hot felsic relaminant and depleted mantle (source of alkaline magmatism) during Permian times and its redistribution associated with growth of the orocline. All these studies are in agreement with massive mantle and lower crustal fluxes parallel to the axial planes of the orocline and perpendicular to the general shortening direction as shown in this study. These structures can be well seen in Fig. 11 and 12, where narrow vertical cusps can be observed. These lower crustal fluxes resemble those reported in orogen parallel extrusions known from Tibet (Dewey, 1988; Zhang et al., 2004; Zheng et al., 2006) and the Eastern Alps (Ratschbacher et al., 1991a,b). In contrast to these collisional systems that require the existence of a free lateral boundary represented by a retreating subduction zone, in our system the

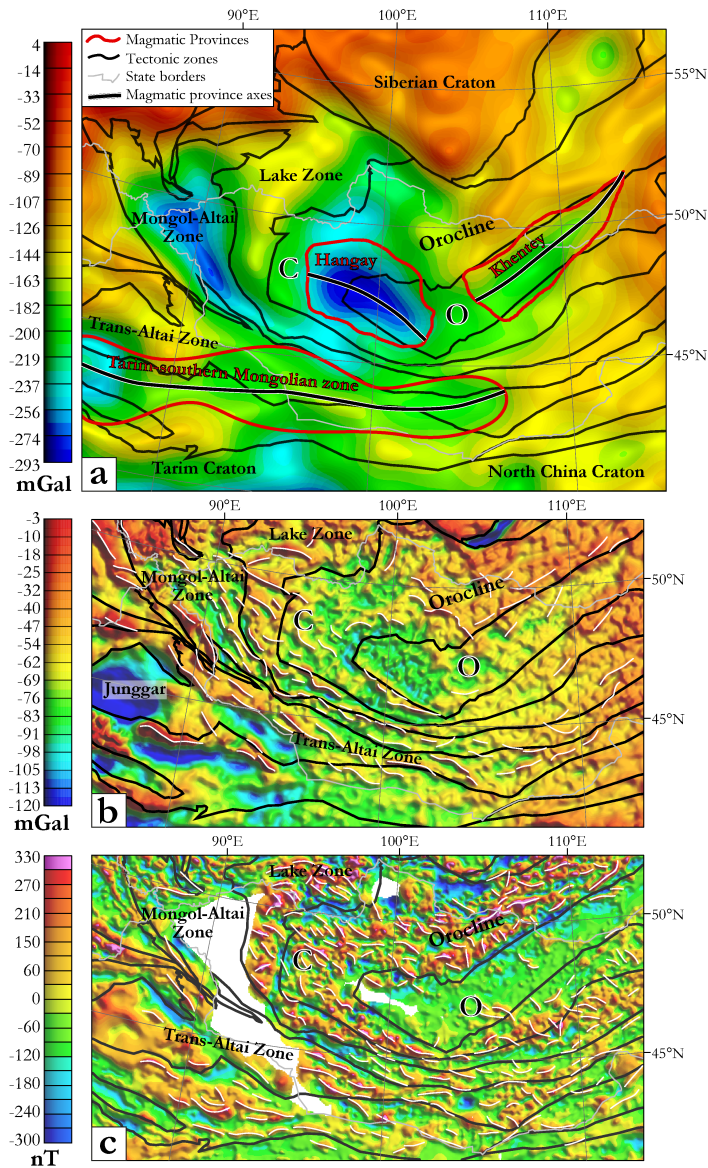


Fig. 17: Geophysical maps used as a likely support of a massive redistribution of the lower crustal material related to the oroclinal bending. (a) Long wavelengths Bouguer gravity anomaly map calculated from EGM08 (Pavlis et al., 2012). The cutoff wavelengths applied is 200 km. The figure shows three major gravity lows related to defined magmatic provinces: the Hangay, Khentey (Yarmolyuk et al., 2013) and Tarim-southern Mongolia magmatic zone (Economos et al., 2012). These alkaline magmatic provinces may result from the melting of elevated mantle and lower crust during oroclinal bend. (b) Isostatic residual gravity anomaly map underlines the distribution of narrow gravity ridges interpreted as zones of intense vertical deformation related to the locking up of oroclinal bend by Guy et al., (2014b). These zones are rooted at 20 km depth (Guy et al., 2015) and may represent proxies of pop down structures modelled in this work. (c) Magnetic anomaly map from EMAG2 (Maus et al., 2009) showing the differences in magnetic signal between low frequency and low amplitude signal in an oceanic domain compared to high frequency and high amplitude signal of continental ribbon domains. Particularly important are narrow magnetic highs related to Permian extrusions of granulite facies material in the Chinese Altai and the shear zones affecting the oceanic crust in Mongolia.

lateral material fluxes are controlled by the active amplification of the oroclinal fold. Finally, a characteristic feature of the Mongolian orocline is a remarkable contrast between a high frequency and amplitude magnetic anomaly signal of the continental ribbons compared to low frequency and amplitude signal of the oceanic domains (Fig. 17c) supporting the main shape of oroclinal bend. Moreover, the development of upright folds with horizontal axes that formed simultaneously with the oroclinal buckling in the continental and oceanic subdomains is observed (Guy et al., 2014a; Lehmann et al., 2010). This folding is best developed in the model surface analysis (Fig. 13). Importantly, the indentation profile expressed in the model may well reflect structural features described recently along the boundary of the Chinese Altai and southerly east Junggar oceanic crust (Jiang et al., 2019; Broussolle et al., 2019).

## 2.6 Conclusions

This study represents a new approach to the simulation of the mechanical processes related with the building of large oroclinal systems that are associated with lateral compression. It investigates mass transfer at the model surface which is responsible for the deformation of the upper crust and for the development of topography, ductile flows inside the model domain and the mechanical coupling in lithospheric multilayer. The main modelling features can be summarized as follows:

- The lateral shortening of the pre-folded accretionary belt leads to development of two regional-scale types of folds: the steeply plunging orocline and the upright folds which form in the oceanic and continental domains with subhorizontal fold axes.
- Generally, all curvilinear fold developed in the upper crust express geometry of the axial planes of upright folds affecting also deeper lithospheric layers.
- The overall deformation distribution shows significant thickening and exhumation of lower ductile layers at the piston side (results of indentation), accommodated by thickening of the upper crustal material at the back-stop side.
- The overthrusting of oceanic crust along one of the orocline hinges (O→C) and continental crust along the other (C→O) is associated with material vortex flow around the inflection of the orocline. This pattern decays towards deeper lithospheric layers, where the lateral flow of material is negligible.
- Our model suggests that the geometry of the orocline is non-cylindrical with increasing plunge of fold axis from upper crust towards deeper lithospheric layers.
- The redistribution of lower crustal and mantle material related to oroclinal buckling is consistent with some geophysical, namely gravity and magnetic data for the Mongolian orocline. In particular, the model may explain formation of a giant gravity low in the hinge zone of the Mongolian orocline that can

coincide with vertical flux of hot mantle and hot lower crust. In addition, the linear zones of gravity highs associated with vertical zones parallel to orocline axial plane may reflect formation of simulated pop-down structures. Finally, the deformation gradient reported along the southern flank of Mongolian orocline may correspond to indentation profile expressed by our model.

## 2.7 Appendix

### 2.7.1 The first generation of experiments

Before we developed the model where a full-wave-length orocline was simulated, the first generation of experiments was performed (Fig. 18). In these models we partly followed the scheme of Pastor-Galán et al. (2012) where the continental ribbon is progressively buckled and developed the architecture of an arcuated orocline with developed orogenic root in the central part of the arc and with large-scale extensional ruptures oriented parallel to the shortening direction. However, in our modelling approach we surrounded the continental ribbon by neutral silicone material (Fig. 18b) and incorporated vertically oriented layers (including driving plastic layer) at the side of the central continental subdomain (Fig. 18a). The model evolution (Fig. 18c) here corresponds more realistically to natural material fluxes which are not separated by discontinuum from surrounding rock materials.

The model domain deformation corresponds to buckling of the driving layer and vertically oriented layers representing an accretionary belt. The axial plane of the developed orocline is characterized by strong hinge indentation through a central continental ribbon (Fig. 18c). Similarly to the second generation of experiments - that are presented above - the significant ascent of the mantle material occur beneath the orocline hinge zone (Fig. 21b). The shear zones with convergence to the hinge zone are partly developed in upper brittle crust in the continental ribbon, however, in comparison to the second generation of experiments, the topography of the models is insignificant.

### 2.7.2 Interlimb areas of the orocline

The topography of the upper crust in a full-wavelength orocline models (the second generation) is significantly affected by pure-shear deformation between both interlimb sectors (Fig. 19). The deformation of the oceanic domain (O→C) is characterized by less significant vertical extrusion of the oceanic mantle which is compensated for by development of pop-down and pop-up structures. In contrast, the continental domain (C→O) is characterized by buckling of horizontal layers in the interlimb sector and upright folding. The pop-down structures are not fully developed in this region while the pop-ups dominate the topography (Fig. 19 - 45-50% shortening).

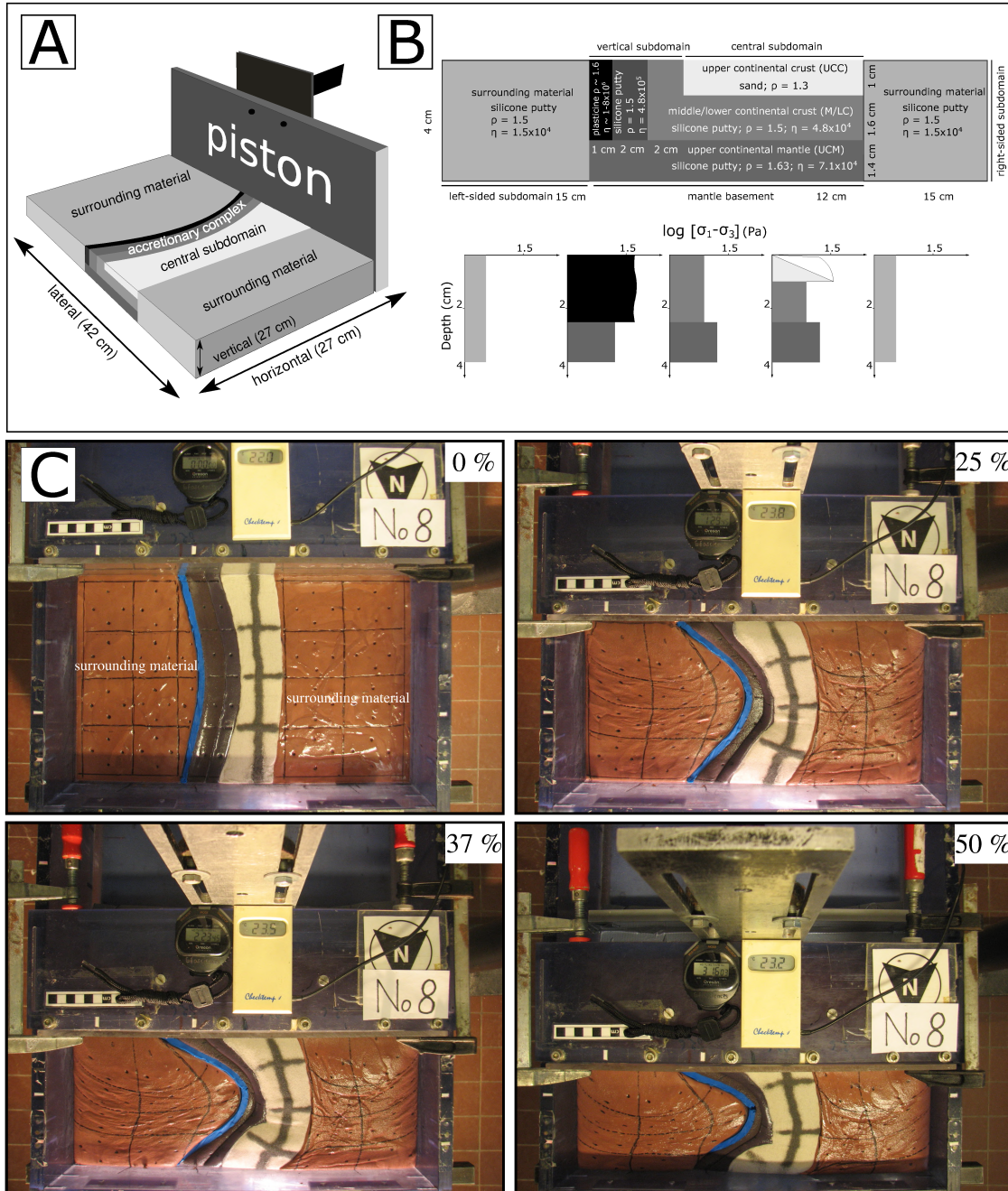


Fig. 18: The first generation of experiments of oroclinal buckling. The geometrical model setup (A) contains half-wave orocline. The model materials with rheological properties and strength profiles are shown at (B). The model evolution with typical buckling of central layers (accretionary complex) is illustrated at (C) for four evolutionary stages.

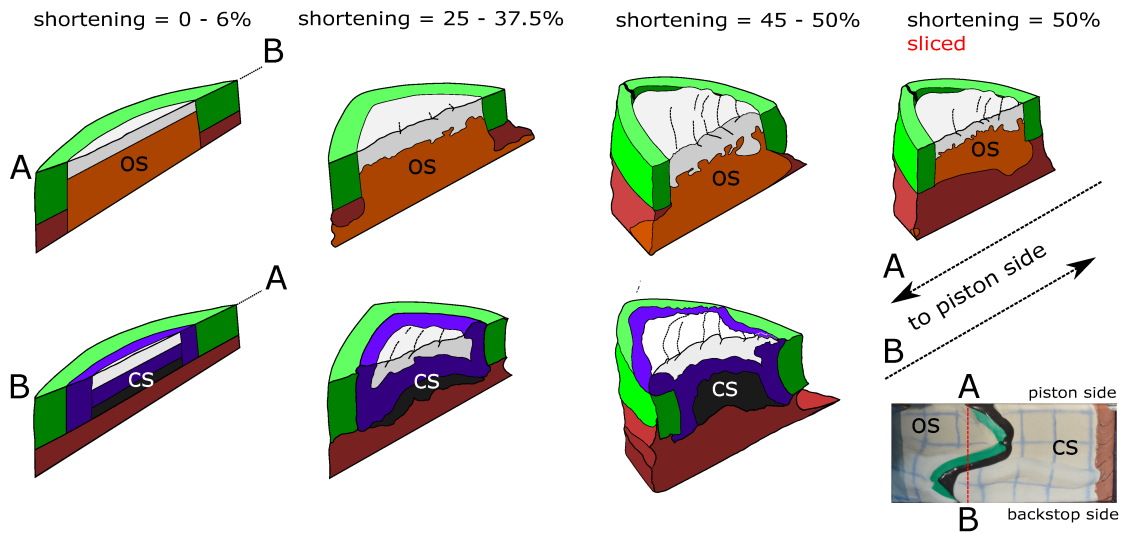


Fig. 19: Evolution of interlimb and hinge orocline sectors for O→C and C→O domains. Both interlimb sectors are reoriented to the same projection direction and orientation respective to piston (indenter) is illustrated by arrows.

### 2.7.3 Velocity components and displacement differences

The components of displacement and velocity field are shown at Fig. 20. The main deformation lines in the model domain correspond to the gradient in displacement field and as its progressively moved from identer side to back-stop side (Fig. 20a). Both horizontal components of the velocity field show a main direction of the material transfer at the top of the model. The velocity azimuth map shows that the dominant direction of the velocity is in C→O sector during ca 10-20% of shortening while for 0-10% shortening the flow is more significant in O→C sector in the reverse direction.

The horizontal displacement in direction of the domain shortening varies for different model subdomains (Fig. 20b). As the model behaves as a system with the Poiseuille type of channel flow (Fig. 20c) the maximum displacement occurs for central (continental) subdomain while oceanic subdomain has a smaller displacement. This is one of the factors that affect asymmetry of pop-down and pop-up belts distribution in the model domain (Fig. 14).

### 2.7.4 General 3D flow

The calculations of the real 3D vlocity data were not possible due to absence of the CT (X-ray) tomography device. For this reason we estimated inner material displacement (Fig. 21) from a series of cross-sections (Fig. 11-20) where we analyzed incremental evolution of deformation features. The reconstructed displacement field is supported by a 2D velocity field which was calculated by the PIV (particle image

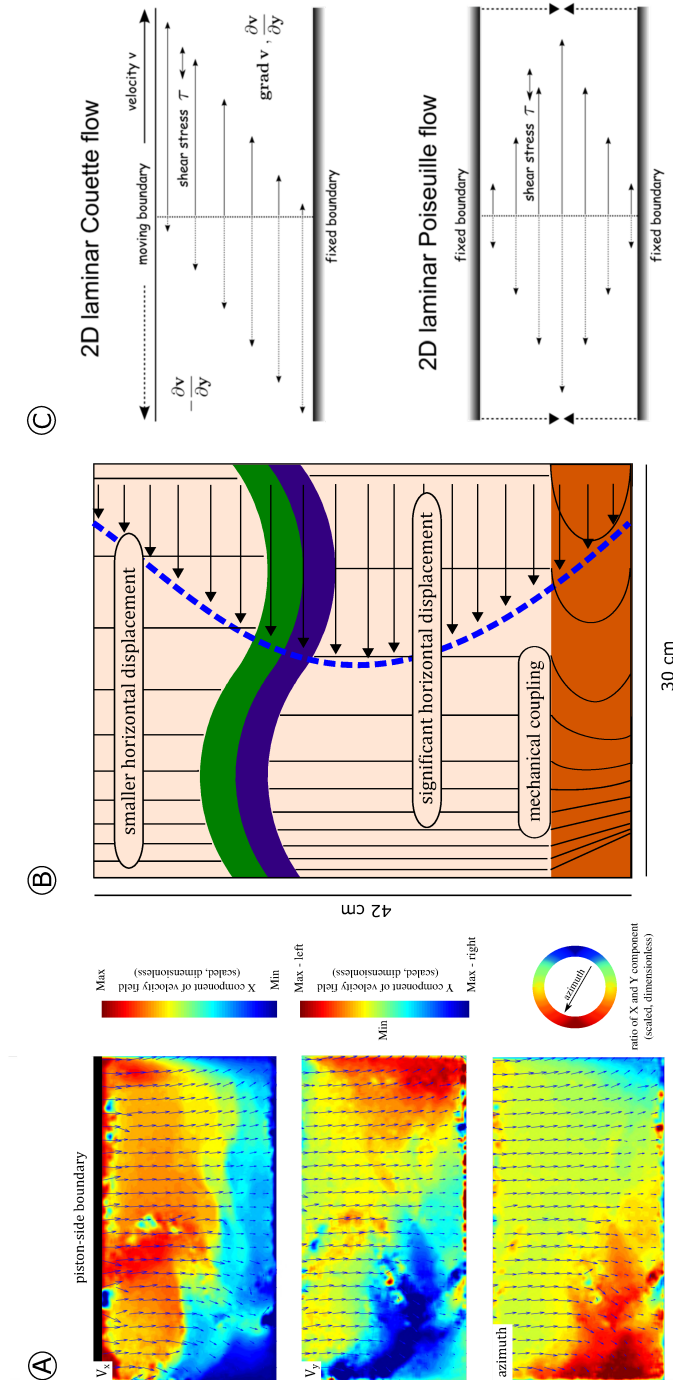


Fig. 20: Velocity components and style of flow in the model domain. (A) representing  $x$  and  $y$  components of the velocity field and calculated azimuth of material transfer.  $X$  component has a highest values distributed close to the indenter while  $y$  component has a maximum in both directions, perpendicularly to the indenter. Colorbar for azimuth distinguish left, central and right direction (illustrated by arrow in colored circle). (B) is a map of the main differences in the displacement for all model subdomains. Dashed line denotes Poiseuille type of channel flow while straight black lines and their spacing illustrate differential displacement. (C) shows two basic types of the channel flow in the model domain, Couette flow and Poiseuille flow and their principle.

velocimetry) method. The 3D reconstruction show main directions and estimated magnitudes of the displacement between material elements in a series of the sections that are oriented in perspective view from indenter through inflection plane to the backstop. The individual stars in the 2D velocity field map corresponds to the main deformation features and velocity anomalies (numbers in brackets in further text).

From 1-10% shortening of the model domain is visible rapid amplification of driving layer (1) with indentation of the hinge and inflow of the material which is situated in interlimb sectors (3,4). The significant deformation of the upper crust in the oceanic and continental domain correlates with a sharp gradient in the velocity field (2,6) and maximum velocity is close to the indenter in a central part of the model domain (5). The velocity gradient is progressively moved from indenter to distal parts (8,10) where the main surface deformation will take a place during later evolutionary stages. The mechanical coupling between surrounding material and continental material occurs during this stage (7). Velocity of the material displacement is homogenized in the wide field between these velocity gradients and indenter side (9). In the lower levels of the continental and oceanic domain this displacement is less significant than in top levels due to the presence of the rigid basal plate at the bottom (scheme of displacement follows Couette style of channel flow).

When the model domain is shortened up to 20-25% the localized areas of high velocities and sharp gradients (11,12) became more distributed (15,16) and development of associated structures in the upper crust (pop-up, pop-down structures, strike-slips etc.) is finished. The amplification of hinge areas (14) and rotation of the material around inflection of orocline (13) are also slowed. The indentation of hinges is responsible for vertical gradient in material displacement (Couette flow) and partial mantle pull from lower levels to continental and oceanic subdomains (Fig. 21 - 3D reconstruction panel).

The late evolutionary stage between 37-50% of domain shortening represents dominantly pure shear deformation with no significant development of topography. The small variations in the velocity field are associated with a thrusting in front of hinge areas (14), material rotation around inflection axis (13,17) and small material transfers between continental domain and surrounding material (18,19). The progressive movement of deformation line (velocity gradients) is documented by an indentation profile of surrounding material (Fig. 21 - 3D reconstruction panel). In the piston side, the material is indenting the continental subdomain while in back-stop part the surrounding material is indented by continental material.

### 2.7.5 Mantle exhumation and Bouguer anomalies in Hangai zone

The model explains to a certain extent the large-scale negative Bouguer anomalies in the Hangai sector of the Tuva-Mongol orocline (Petit et al., 2002) that are probably associated with significant mantle ascent beneath the O→C orocline hinge zone

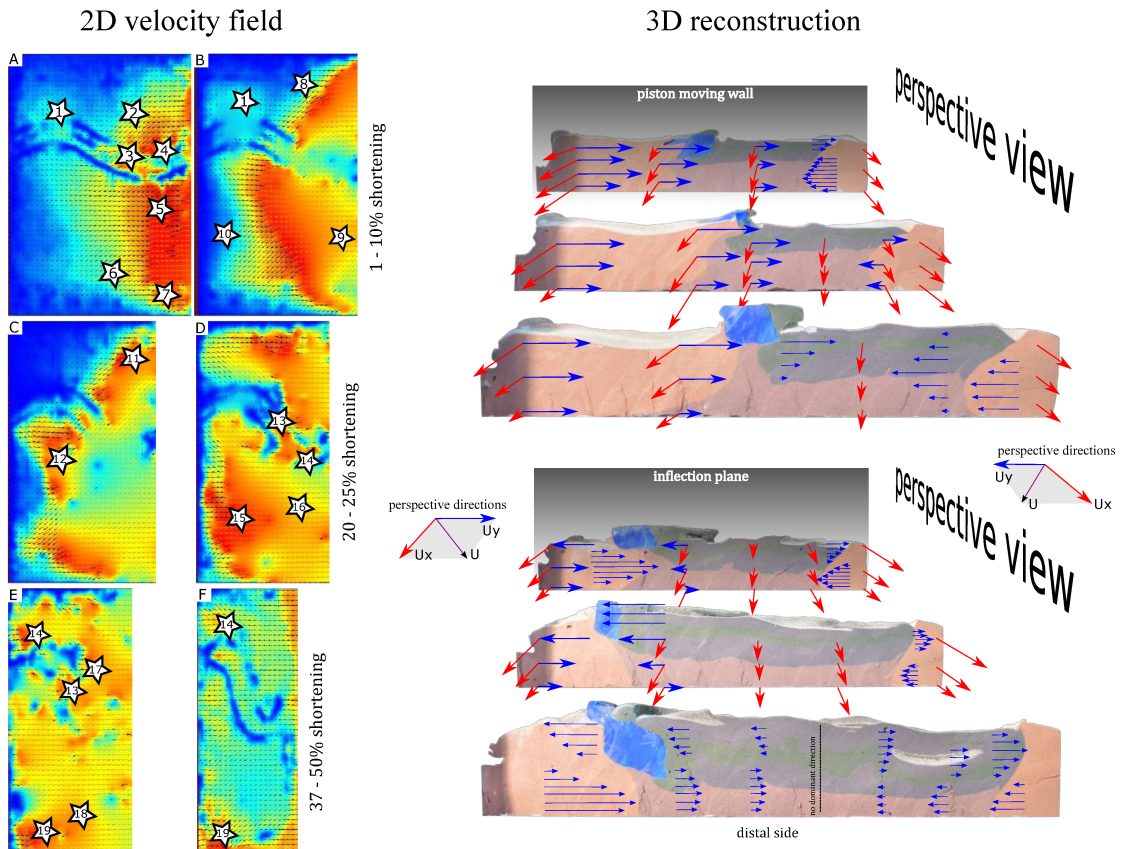


Fig. 21: 2D velocity field was calculated by PIVlab toolbox while 3D reconstruction was derived from sectioned model domain for various finite shortening compared with 2D velocity field. Individual numbers in the small stars represent main flow and deformation features (see text for further explanation). Section in 3D reconstruction are oriented from piston side (upper three sections) through inflection plane to backstop side (lower three sections). All sections and arrows are for illustration of 3D flow oriented in perspective view.

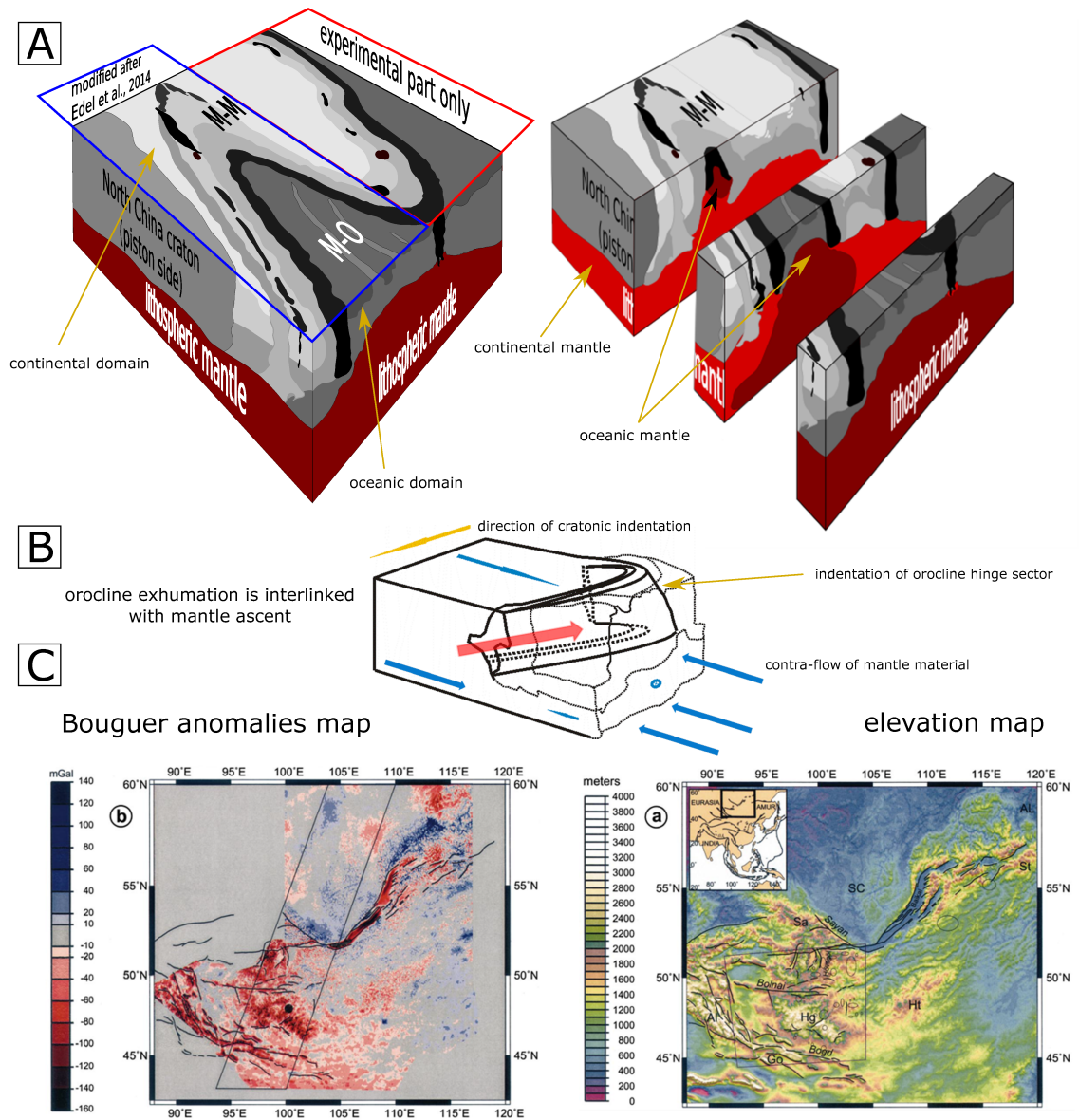


Fig. 22: At the (A) is a block diagram combining the geodynamic model of orocline buckling of Tuva-Mogol orocline (Edel et al., 2014) and presented analogue model. The sectioned diagram shows (as previous analysis confirmed) the oceanic mantle ascent during indentation of North-China craton (piston indenter). The mechanics of the ascent of the pushed and pulled mantle is shown at (B). The corresponding sector in Tuva-Mongol orocline is represented by the Hangai dome (C). Diagrams in (C) show residual Bouguer anomaly map and elevation map for Hangai sector (taken from Petit et al., 2002).

(Fig. 22). The block-diagram (Fig. 22a) combines schematics that are modified after Edel et al., 2014 and the presented model. From the sections it is visible how continental and oceanic mantle lithosphere is cambered beneath interlimb zone of arcuated accretionary complex with the most exhumed part situated underneath the hinge sector. This also corresponds to the vertically rotated orocline (Fig. 22b) which is responsible for mantle pull and flow-up. The presence of hot mantle material may be responsible for partial melting of the lower crustal rocks as well as the mantle itself experienced decompression and underwent partial melting. Decreasing regional density of rock material then affects the distribution of light material and negative values of Bouguer anomalies.

## 2.8 Acknowledgments

*This paper was supported by the Czech Science Foundation grant No.: 17-17540S, National Natural Science Foundation of China (41888101), and the Center for Geosphere Dynamics project UNCE/SCI/006. We thank to J. J. Kermarrec for his help in the modeling laboratory at Géosciences Rennes, University of Rennes 1, France. Primary data for: Oroclinal buckling and associated lithospheric-scale material flow - insights from physical modeling: implication for Mongolian orocline" are available on <https://dataverse.harvard.edu/dataset.xhtml?persistentId=doi:10.7910/DVN/QNFHDO>, Harvard Dataverse*

## 2.9 References

- Beaumont, C., Jamieson, R. A., Nguyen, M. H., and Medvedev, S. (2004). Crustal channel flows: 1. Numerical models with applications to the tectonics of the Himalayan-Tibetan orogen. *Journal of Geophysical Research: Solid Earth*, 109(B6).
- Beaumont Ch., Nguyen M. H., Jamieson R. A. and Ellis S. (2006) Crustal flow modes in large hot orogens. Geological Society, London, Special Publications, 268, 91-145.
- Boutelier D., Schrank C., Cruden A. (2008) Power-law viscous materials for analogue experiments: New data on the rheology of highly-filled silicone polymers. *Journal of Structural Geology*, 30, 341-353.
- Boutelier D., Oncken O., Cruden A.R. (2014) Trench-parallel shortening in the forearc caused by subduction along a seaward-concave plate boundary: Insights from analogue modelling experiments. *Tectonophysics*, 611, 192-203.
- Boutelier, D., Gagnon, L., Johnston, S., and Cruden, A. (2018). Buckling of orogens: Insights from analogue modelling. *Journal of Structural Geology*, In Press

(DOI: 10.1016/j.jsg.2018.02.005)

Broussolle, A., M. Sun, K. Schulmann, A. Guy, C. Aguilar, P. Štípská, Y. Jiang, Y. Yu, and W. Xiao (2019), Are the Chinese Altai “terrane” the result of juxtaposition of different crustal levels during Late Devonian and Permian orogenesis?, *Gondwana Research*, 66, 183-206

Broussolle, A., Aguilar, C., Sun, M., Schulmann, K., Štípská, P., Jiang, Y., Yu, Y., Xiao, W. and Míková, J. (2018). Polycyclic Palaeozoic evolution of accretionary orogenic wedge in the southern Chinese Altai: Evidence from structural relationships and U–Pb geochronology. *Lithos*, 314, 400-424.

Brun J.-P. (2002) Deformation of the continental lithosphere: Insights from brittle-ductile models. Geological Society, London, Special Publications, 200, 355-370.

Buiter S. J. H. and Schreurs G. (eds) (2006) Analogue and Numerical Modeling of Crustal-Scale Processes. Geological Society, London, Special Publications, 253.

Burg, J.P., Nievergelt, P., Oberli, F., Seward, D., Davy, P., Maurin, J.C., Diao, Z. and Meier, M. (1998) The Namche Barwa syntaxis: evidence for exhumation related to compressional crustal folding. *Journal of Asian Earth Sciences*, 16(2-3), pp.239-252.

Byerlee J. (1978) Friction of rocks. *Pure and Applied Geophysics*, 116, 615-626.

Cagnard F., Brun J.-P., Gapais D. (2006) Modes of thickening of analogue weak lithospheres. *Tectonophysics*, 421, 145–160.

Cobbold, P.R. and Jackson M.P.A. (1992) Gum rosin (colophony): A suitable material for thermomechanical modeling of the lithosphere. *Tectonophysics*, 210, 255–271.

Cocks, L. R. M., and Torsvik, T. H. (2007). Siberia, the wandering northern terrane, and its changing geography through the Palaeozoic. *Earth-Science Reviews*, 82(1-2), 29-74.

Davy P. and Cobbold P. R. (1988) Indentation tectonics in nature and experiment. 1. Experiments scaled for gravity. *Bulletin of the Geological Institutions of Uppsala*, 14, 129-141.

Davy, P. and Cobbold, P. R. (1991) Experiments on shortening of a 4-layer model of the continental lithosphere. *Tectonophysics*, 188, 1–25.

Dewey, J. F., Shackleton, R. M., Chengfa, C., and Yiyin, S. (1988). The tec-

tonic evolution of the Tibetan Plateau. *Phil. Trans. R. Soc. Lond. A*, 327(1594), 379-413.

Duretz, T., Kaus, B. J. P., Schulmann, K., Gapais, D., and Kermarrec, J. J. (2011). Indentation as an extrusion mechanism of lower crustal rocks: Insight from analogue and numerical modeling, application to the Eastern Bohemian Massif. *Lithos*, 124(1), 158-168.

Edel J.-B., Schulmann K., Hanžl P., Lexa O. (2014) Palaeomagnetic and structural constraints on 90° anticlockwise rotation in SW Mongolia during the Permo-Triassic: implications for Altaid oroclinal bending. *Journal of Asian Earth Sciences*, 94, 157–171.

England, P., and Houseman, G. (1986). Finite strain calculations of continental deformation: 2. Comparison with the India-Asia collision zone. *Journal of Geophysical Research: Solid Earth*, 91(B3), 3664-3676.

England, P., and Houseman, G. (1989). Extension during continental convergence, with application to the Tibetan Plateau. *Journal of Geophysical Research: Solid Earth*, 94(B12), 17561-17579.

Gaggero, L., Marroni, M., Pandolfi, L., and Buzzi, L. (2009). Modeling of oceanic lithosphere obduction: constraints from the metamorphic sole of Mirdita ophiolites (Northern Albania). *Ofioliti*, 34(1), 17-42.

Galland, O., Bertelsen, H. S., Guldstrand, F., Girod, L., Johannessen, R. F., Bjugger, F., ... and Mair, K. (2016). Application of open-source photogrammetric software MicMac for monitoring surface deformation in laboratory models. *Journal of Geophysical Research: Solid Earth*, 121(4), 2852-2872.

Gerya, T., and Stöckhert, B. (2006). Two-dimensional numerical modeling of tectonic and metamorphic histories at active continental margins. *International Journal of Earth Sciences*, 95(2), 250-274.

Gerya, T. (2014). Precambrian geodynamics: concepts and models. *Gondwana Research*, 25(2), 442-463.

Gutiérrez-Alonso, G., Johnston, S. T., Weil, A. B., Pastor-Galán, D., and Fernández-Suárez, J. (2012). Buckling an orogen: The Cantabrian Orocline. *GSA Today*, 22(7), 4-9.

Guy A., Schulmann K., Clauer N., Hasalová P., Seltmann R., Armstrong R., Lexa O., Benedicto A. (2014) Late Paleozoic–Mesozoic tectonic evolution of the Trans-Altai

and South Gobi Zones in southern Mongolia based on structural and geochronological data. *Gondwana Research*, 25, 309–337.

Guy, A., Schulmann, K., Munschy, M., Mieke, J. M., Edel, J. B., Lexa, O., and Fairhead, D. (2014). Geophysical constraints for terrane boundaries in southern Mongolia. *Journal of Geophysical Research: Solid Earth*, 119(10), 7966–7991.

Guy, A., Schulmann, K., Janoušek, V., Štípská, P., Armstrong, R., Belousova, E., ... and Hanzl, P. (2015). Geophysical and geochemical nature of relaminated arc-derived lower crust underneath oceanic domain in southern Mongolia. *Tectonics*, 34(5), 1030–1053.

Hubbert M.K. (1937) Theory of scale models as applied to the study of geological structures. *Geological Society of America Bulletin*, 48, 1459–1520.

Jiang, Y.D., Schulmann, K., Sun, M., Štípská, P., Guy, A., Janoušek, V., Lexa, O. and Yuan, C. (2016) Anatexis of accretionary wedge, Pacific-type magmatism, and formation of vertically stratified continental crust in the Altai Orogenic Belt. *Tectonics*, 35(12), pp.3095–3118.

Jiang, Y.D., Schulmann, K., Kröner, A., Sun, M., Lexa, O., Janoušek, V., Buriánek, D., Yuan, C. and Hanzl, P. (2017) Neoproterozoic-Early Paleozoic Peri-Pacific Accretionary Evolution of the Mongolian Collage System: Insights From Geochemical and U-Pb Zircon Data From the Ordovician Sedimentary Wedge in the Mongolian Altai. *Tectonics*, 36(11), pp.2305–2331.

Jiang, Y. D., Schulmann, K., Sun, M., Weinberg, R. F., Štípská, P., Li, P.F., Zhang, J., Chopin, F., Wang, S., Xia, X. P., Xiao, W. J. (2019) Structural and Geochronological Constraints on Devonian Suprasubduction Tectonic Switching and Permian Collisional Dynamics in the Chinese Altai, Central Asia. *Tectonics*, 38(1), 253–280.

Kovalenko, V. I., Yarmolyuk, V. V., Kovach, V. P., Kotov, A. B., Kozakov, I. K., Salnikova, E. B., and Larin, A. M. (2004). Isotope provinces, mechanisms of generation and sources of the continental crust in the Central Asian mobile belt: geological and isotopic evidence. *Journal of Asian Earth Sciences*, 23(5), 605–627.

Koyi, H. A. and Mancktelow, N. S. (2001) *Tectonic Modeling: A Volume in Honor of Hans Ramberg*. Geological Society of America, 193.

Krýza, O., Závada, P., Lexa, O. (2019) Advanced strain and mass transfer analysis in crustal-scale oroclinal buckling and detachment folding analogue models. *Tectonophysics*, In Press (DOI: 10.1016/j.tecto.2019.05.001).

- Lehmann J., Schulmann K., Lexa O., Corsini M., Kröner A., Štípská P., Tomurhuu D. and Otgonbator D. (2010) Structural Constraints of the Evolution of the Central Asian Orogenic Belt in sw Mongolia. *American Journal of Science*, 310, 575–628.
- Li, Z. L., H. L. Chen, S. F. Yang, C. W. Dong, W. J. Xiao, J. L. Li, Y. Ye, and J. Wang (2004), Discovery and genetic mechanism of basic granulite in the Altay orogenic belt, Xinjiang, NW China, *Acta Geologica Sinica-English Edition*, 78, 177-185.
- Luján, M., Rossetti, F., Storti, F., Ranalli, G., and Socquet, A. (2010). Flow trajectories in analogue viscous orogenic wedges: Insights on natural orogens. *Tectonophysics*, 484(1), 119-126.
- Maierová, P., Čadek, O., Lexa, O., and Schulmann, K. (2012). A numerical model of exhumation of the orogenic lower crust in the Bohemian Massif during the Variscan orogeny. *Studia Geophysica et Geodaetica*, 56(2), 595-619.
- Maierová, P., Lexa, O., Schulmann, K., and Štípská, P. (2014). Contrasting tectono-metamorphic evolution of orogenic lower crust in the Bohemian Massif: a numerical model. *Gondwana Research*, 25(2), 509-521.
- Maierová, P., Schulmann, K., and Gerya, T. (2018). Relamination Styles in Collisional Orogens. *Tectonics*, 37(1), 224-250.
- Maus, S., et al. (2009), EMAG2: A 2-arc min resolution Earth Magnetic Anomaly Grid compiled from satellite, airborne, and marine magnetic measurements, *Geochemistry, Geophysics, Geosystems*, 10(8)
- Meffre, S., Berry, R. F., and Hall, M. (2000). Cambrian metamorphic complexes in Tasmania: tectonic implications. *Australian Journal of Earth Sciences*, 47(6), 971-985.
- Menant, A., Sternai, P., Jolivet, L., Guillou-Frottier, L., and Gerya, T. (2016). 3D numerical modeling of mantle flow, crustal dynamics and magma genesis associated with slab roll-back and tearing: The eastern Mediterranean case. *Earth and Planetary Science Letters*, 442, 93-107.
- Midtkandal, I., Brun, J. P., Gabrielsen, R. H., and Huisman, R. S. (2013). Control of lithosphere rheology on subduction polarity at initiation: Insights from 3D analogue modeling. *Earth and Planetary Science Letters*, 361, 219-228.
- Nguyen, H., Hanžl, P., Janoušek, V., Schulmann, K., Ulrich, M., Jiang, Y., Lexa, O., Altanbaatar, B. and Deiller, P. (2018) *Geochemistry and geochronology of Mis-*

Mississippian volcanic rocks from SW Mongolia: Implications for terrane subdivision and magmatic arc activity in the Trans-Altai Zone. *Journal of Asian Earth Sciences*, 164, pp.322-343.

Pastor-Galán D., Gutiérrez-Alonso G., Zulauf G. and Zanella F. (2012) Analogue modeling of lithospheric-scale oroclinal buckling: Constraints on the evolution of the Iberian-Armorican Arc. *Geological Society of America Bulletin*, 124, 1293-1309.

Pavlis, N. K., S. A. Holmes, S. C. Kenyon, and J. K. Factor (2012), The development and evaluation of the Earth Gravitational Model 2008 (EGM2008), *Journal of Geophysical Research: Solid Earth*, 117(B4)

Petit, C., Déverchère, J., Calais, E., San'kov, V., and Fairhead, D. (2002). Deep structure and mechanical behavior of the lithosphere in the Hangai–Hövsgöl region, Mongolia: new constraints from gravity modeling. *Earth and Planetary Science Letters*, 197(3-4), 133-149.

Ramberg H. (1981) *Gravity, Deformation and the Earth Crust*. Academic Press, London and New York.

Ratschbacher L., Merle O., Davy P. and Cobbold P. R. (1991) Lateral extrusion in the Eastern Alps, Part 1: Boundary conditions and experimental experiments scaled for gravity. *Tectonics*, 10, 245-256.

Ratschbacher, L., Frisch, W., Linzer, H. G., and Merle, O. (1991). Lateral extrusion in the Eastern Alps, part 2: structural analysis. *Tectonics*, 10(2), 257-271.

Rosenbaum, G. (2012). Oroclines of the southern New England orogen, eastern Australia. *Episodes*, 35(1), 187-194.

Rosenbaum, G. (2014). Geodynamics of oroclinal bending: Insights from the Mediterranean. *Journal of Geodynamics*, 82, 5-15.

Rosenbaum, G., and Lister, G. S. (2004). Formation of arcuate orogenic belts in the western Mediterranean region. *Geological Society of America Special Papers*, 383, 41-56.

Schöpfer M. P. J. and Zulauf G. (2002) Strain-dependent rheology and the memory of plasticity. *Tectonophysics*. 354, 85 – 99.

Seltmann, R., D. Konopelko, G. Biske, F. Divaev, and S. Sergeev (2011), Hercynian post-collisional magmatism in the context of Paleozoic magmatic evolution of the Tien Shan orogenic belt, *Journal of Asian Earth Sciences*, 42(5), 821-838

- Slagstad, T., Pin, C., Roberts, D., Kirkland, C. L., Grenne, T., Dunning, G., Sauer, S. and Andersen, T. (2014). Tectonomagmatic evolution of the Early Ordovician suprasubduction-zone ophiolites of the Trondheim Region, Mid-Norwegian Caledonides. *Geological Society, London, Special Publications*, 390(1), 541-561.
- Şengör, A. M. C., Natal'In, B. A., and Burtman, V. S. (1993). Evolution of the Altaid tectonic collage and Palaeozoic crustal growth in Eurasia. *Nature*, 364(6435), 299.
- Sengör, A. C., and Natal'In, B. A. (1996). Turkic-type orogeny and its role in the making of the continental crust. *Annual Review of Earth and Planetary Sciences*, 24(1), 263-337.
- Tapponier P., Peltzer G., Le Dain Y., Armijo R. and Cobbold P. (1982) Propagating extrusion tectonics in Asia: New insights from simple experiments with plasticine. *Geology*, 10, 611-616.
- Thielicke, W., and Stamhuis, E. (2014). PIVlab—towards user-friendly, affordable and accurate digital particle image velocimetry in MATLAB. *Journal of Open Research Software*, 2(1).
- Tikoff, B., Teyssier, C., and Waters, C. (2002). Clutch tectonics and the partial attachment of lithospheric layers. *EGU Stephan Mueller Special Publication Series*, 1, 57-73.
- Thompson, A. B., Schulmann, K., Jezek, J., and Tolar, V. (2001). Thermally softened continental extensional zones (arcs and rifts) as precursors to thickened orogenic belts. *Tectonophysics*, 332(1-2), 115-141.
- Tomurtogoo, O., Windley, B. F., Kröner, A., Badarch, G., and Liu, D. Y. (2005). Zircon age and occurrence of the Adaatsag ophiolite and Muron shear zone, central Mongolia: constraints on the evolution of the Mongol–Okhotsk ocean, suture and orogen. *Journal of the Geological Society*, 162(1), 125-134.
- Weil, A. B., Van der Voo, R., and van der Pluijm, B. A. (2001). Oroclinal bending and evidence against the Pangea megashear: The Cantabria-Asturias arc (northern Spain). *Geology*, 29(11), 991-994.
- Wilhem, C., Windley, B. F., and Stampfli, G. M. (2012). The Altaids of Central Asia: a tectonic and evolutionary innovative review. *Earth-Science Reviews*, 113(3-4), 303-341.
- Xiao, W., B. Windley, S. Sun, J. Li, B. Huang, C. Han, C. Yuan, M. Sun, and H.

Chen (2015), A tale of amalgamation of three collage systems in the Permian-Middle Triassic in Central Asia: Oroclines, sutures and terminal accretion, *Annual Review of Earth and Planetary Sciences*, 43, 477-507

Xiao, W., Windley, B.F., Han, C., Liu, W., Wan, B., Zhang, J.E., Ao, S., Zhang, Z. and Song, D. (2018) Late Paleozoic to early Triassic multiple roll-back and oroclinal bending of the Mongolia collage in Central Asia. *Earth-Science Reviews*, 186, pp.94-128.

Yakubchuk, A. S. (2005). Gold and base metal metallogeny of the Central Asian orogenic supercollage. *Econ. Geol.*, 100, 1035-1068.

Yarmolyuk, V. V., Kudryashova, E. A., Kozlovsky, A. M., and Savatenkov, V. M. (2007). Late Cretaceous-Early Cenozoic volcanism of Southern Mongolia: A trace of the South Khangai mantle hot spot. *Journal of Volcanology and Seismology*, 1(1), 1-27.

Zhang, P.Z., Shen, Z., Wang, M., Gan, W., Bürgmann, R., Molnar, P., Wang, Q., Niu, Z., Sun, J., Wu, J. and Hanrong, S. (2004) Continuous deformation of the Tibetan Plateau from global positioning system data. *Geology*, 32(9), pp.809-812.

Zheng, D., Zhang, P.Z., Wan, J., Yuan, D., Li, C., Yin, G., Zhang, G., Wang, Z., Min, W. and Chen, J. (2006). Rapid exhumation at 8 Ma on the Liupan Shan thrust fault from apatite fission-track thermochronology: Implications for growth of the northeastern Tibetan Plateau margin. *Earth and Planetary Science Letters*, 248(1-2), pp.198-208.



### 3 Advanced strain and mass transfer analysis in crustal-scale oroclinal buckling and detachment folding analogue models

Ondřej Krýza, Prokop Závada and Ondrej Lexa

#### 3.1 Abstract

The PIV (particle image velocimetry) method became a standard tool for the calculation of displacement fields in physical geodynamic models. For understanding the deformation dynamics of geodynamic models, in our study, we implemented several post-processing algorithms on the derived displacement field and calculated the velocity and strain(-rate) components, such as the divergence of the velocity field, vorticity and shear strain-rate.

In the model of oroclinal buckling, we focused on strain analysis of the upper crust and correlated the shear strain-rate, vorticity and divergence anomalies with visual deformation patterns in the upper crust. The divergence of velocity fields in these models correspond to the pop-up and pop-down belts oriented along the axial trace of the oroclinal bends. High shear strain-rate domains correlate with horizontal, isovolumic shear zones alongside these belts, while vorticity shows rotational trend of fold axial traces of the pop-up and pop-down belts, around oroclinal inflection.

In another series of models, we simulated the development of melt-cored crustal scale detachment folds and employed the same set of parameters to investigate the ductile deformation visible in side-view of the model domain. We developed a method that allows tracing the divergence in subcells locked on target subdomains. We tracked and quantified melt flow between the melt source area at the bottom of the model and progressively developing folds. This mass transfer analysis revealed polyphase fold evolution, where initial fold perturbations quickly amplify as the melt accumulates in the triangular hinge sector below and between the rotating fold limbs. While the early amplification leads to decompression driving the melt into the hinge zone area between the limbs, the fold lock-up stage and continued attenuation of the vertical limbs is associated with melt expulsion from the fold interlimb domain back into the source layer, where it can be transferred laterally to the foreland.

**Keywords:** analogue modelling, PIV method, oroclinal buckling, detachment folding, strain-rate, divergence

#### Highlights:

- Models of oroclinal buckling and detachment folding were investigated by the PIV method.

- Several model parameters related to the velocity and strain were used to analyze the deformation features in both models.
- The divergence of the velocity field reflects distortion of the model surface.
- Analysis of the divergence reflects mass transfer budget in detachment folds.
- The fold growth rate is driven by the degree of melt flux into the axial zone.

## 3.2 Introduction

Analogue modelling represents a powerful tool for understanding geodynamic processes and therefore requires precise analysis of internal kinematics and deformation. The PIV (particle image velocimetry) technique is often employed to calculate the displacement/velocity field in the models to understand the model evolution on a global scale (e.g. Adrian, 2005; Adam et al., 2005; Krézsek et al., 2007; Schmatz et al., 2010; Warsitzka et al., 2013; Adam et al., 2013; Kettermann and Urai, 2015; Kettermann et al., 2016; Schellart and Strak, 2016; Boutelier, 2016). The core of the PIV method is based on tracing individual image elements (image patterns that consist of a specific arrangement of individual pixels or voxels) in the time-sequence of images (Fig. 23). Displacement vectors are then calculated on the basis of redistribution of these elements between the time steps. High resolution, fast calculations and relatively simple implementation of advanced scripting for data post-processing (vector validation, visualization, data smoothing) qualify the PIV method for deformation analysis of various physical laboratory models, especially for geometrically and rheologically complex simulations associated with high gradients in the velocity field (Adam et al., 2005; Krézsek et al., 2007; Schellart and Strak, 2016).

There are two major types of PIV methods employed in the analogue geodynamical modelling (e.g. Adam et al., 2005; Adam et al., 2013; Boutelier, 2016). First, the 2D PIV technique, which uses images recorded from one camera focused on a single plane, for example, the side-view or plan-view of thin-sheet experiments (e.g. Bajolet et al., 2012; Jang and Lee, 2008). The second type represents the stereoscopic and 3D PIV technique. The stereoscopic PIV technique enables calculating the surface velocity field with three velocity components (e.g. Hori and Sakakibara, 2004; Strak and Schellart, 2014) by tracking and correlating the image elements in photographs collected from several cameras targeted at the model domain from different angles. In contrast, the 3D PIV technique allows to compute the velocity components in a 3D space that consists of voxels (real 3D data), provided by e.g. CT scans, X-ray tomography etc. (e.g. Okamoto et al., 2000; Elsinga et al., 2007; Adam et al. 2013). For the 2D PIV technique, there are several open source software (PIVlab, openPIV, GeoPIV, MatPIV, PIVMat, etc.) or commercial platforms (e.g. LaVision - FlowMaster or StrainMaster, Dantec Dynamics - DynamicStudio, PIV 2D - Imagesystems, etc.). Similarly, for the stereo-PIV methods, that are usually

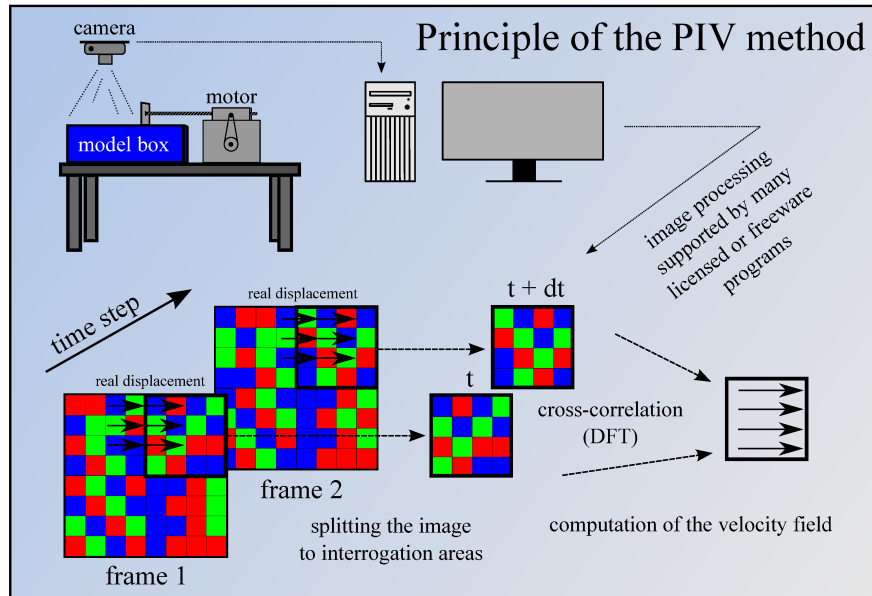


Fig. 23: Simplified scheme of the particle image velocimetry (PIV) analysis principle.

associated with specific camera systems, reconstruction of the surface displacement field can be provided by commercial software (e.g. DaVis from LaVision, etc.) or structure from motion (SfM) methods employing digital elevation models (DEM) that run on commercial platforms, such as Agisoft or open-source software, such as VisualSfM or MicMac (e.g. Galland et al., 2016). The displacement fields obtained from both PIV approaches (2D PIV and stereo-PIV) allow derivation of several model parameters that are associated directly with the velocity field or with strain(-rate) tensor describing the deformation in the model domain that help to quantify the kinematic evolution of the model and its internal dynamics.

Our study aims to illustrate the potential of the 2D PIV method for investigation of the surface deformation in complex analogue models of oroclinal buckling and inner mass transfer dynamics and material deformation in thin-sheet models of crustal-scale detachment folding. To calculate the displacement field, we employed the opensource PIVlab software that represents a good solution for analogue modelling laboratories that are not equipped with commercial systems (e.g. LaVision etc.). In both experiments, we used the calculated displacement field for the derivation of several model parameters, namely the velocity magnitude, shear strain(-rate), the divergence of the velocity field and vorticity and correlate their magnitude with observed deformation structures in the models. While the magnitude of the velocity field simply shows a gradient in displacement rate, the divergence of the velocity field in a plane represents local volumetric changes. Deformation-rate (shear-rate) of the crustal material, represented by the second invariant of the deviatoric strain(-rate) tensor (e.g. Gerya, 2009), corresponds to the isovolumic deformation independently of the global reference frame. The shear strain(-rate) is commonly expressed as

the *xy* component of the strain-tensor in analogue models that operates with the PIV method (e.g. Adam et al., 2005; Warsitzka et al., 2013; Chen et al., 2016). The vorticity of the velocity field (e.g. Schmatz et al., 2010; Bajolet et al., 2012; Warsitzka et al., 2013; Kettermann and Urai, 2015) displays a rotational trend of the material in the model domain.

The geometry of the first model is controlled by amplification of an orocline ribbon that influences the deformation of brittle upper crust and underlying ductile layers. We studied the deformation of the upper crust, marked by folds, strike-slip faults and development of thrusts and normal faults bounding the pop-up and pop-down systems, respectively. For mapping of the compression/extension subdomains related with the development of pop-up and pop-down belts in the upper-crust, we used the divergence of velocity field captured from the top-view of the model surface. This approach is sometimes used in analogue models that produce faults or thrusts (e.g. Reiter et al., 2011; Kettermann et al., 2016) or in models of subduction, where the lower plate is progressively undulated (e.g. Bajolet et al., 2012). Simple shear deformation is mapped by the isovolumic strain invariant and corresponds to strike-slips zones in the deformed model surface, developed in particular along the interface between the orocline and the surrounding material and along some of the pop-up or pop-down belts. The vorticity of the velocity field revealed progressive curvature of originally linear deformation features and rotation around the inflection point of the orocline.

In the second type of the model, the same model parameters serve for tracing the relative mass transfers in side-view of the model domain. This thin sheet experiment is designed to produce a series of crustal scale folds that are developed as a result of the buckling above a melt weakened lower crustal detachment layer. Here, the divergence is employed for tracing the local material flux between the pre-defined subdomains. The mass-transfer calculations required the implementation of additional routines that allow tracing the evolution of divergence in progressively geometrically modified subgrids.

### **3.3 Models of oroclinal buckling**

#### **3.3.1 Model background and setup**

The first type of experiments were constructed in order to understand the relative mass transfers between the different lithospheric domains during oroclinal buckling. Formation of large arcuated orogens is related with rapid topography development associated with deformation of the upper crust (e.g. Pastor-Galán et al., 2012; Rosenbaum, 2012; Rosenbaum and Donchak, 2012; Rosenbaum, 2014), while middle to lower ductile crust is transferred laterally by gravity-driven flow or emplacement of a new material from the subduction wedge (Beaumont et al., 2006;

Pastor-Galán et al., 2012; Maierová et al., 2014, Menant et al., 2016; Maierová et al., 2018).

The model aims to mimic the formation of the Tuva-Mongol orocline (Xiao et al., 2015) after subduction of the Mongol-Okhotsk oceanic plate underneath the Mongolian microcontinent (Lehmann et al., 2010; Edel et al., 2014). The model is designed to simulate the amplification of a preexisting, gently folded, accretionary-subduction system surrounded by two neighbouring oceanic and continental lithospheric sub-domains (Fig. 24a). In general, oroclinal buckling can be considered as a specific type of indentation tectonics setting which is accompanied with lateral movements of individual oroclinal hinges perpendicular to the movements of oceanic/continental blocks. Except for the complex material transfer in deeper lithospheric levels, deformation of the upper crust and related topography development represents an important part of the mechanical behaviour of such a system. The PIV technique was employed for deformation and displacement analysis of the model surface (upper crust) that is controlled by the deep material flows and mechanical coupling between the lithospheric mantle and the crust.

### 3.3.2 Model materials

The upper crust, in both oceanic and continental domains, is simulated by cohesionless Fontainebleau sand (Fig. 24a, Tab. 1). Silicone putties of various viscosity and density (GS1R gum from Rhone Poulenc, France) were used to simulate the ductile lower crust, continental lithospheric mantle and oceanic lithospheric mantle. Mechanical anisotropy in the model was implemented by incorporation of a plasticine layer between the two lithospheric domains as a beam to induce the oroclinal buckling and related mass redistribution. The inserted plasticine layer was pre-folded and represents an artificial element that controls the progressive amplification of the single wavelength orocline.

The model was scaled according to the standard modeling techniques (Hubbert, 1937) and uses the materials with physical properties that are comparable with the materials used in some of the previous 4-layer models (scaling according to Davy and Cobbold (1991) and Brun (2002) and material used according to Cagnard et al. (2006)), except for the incorporated plasticine layer (for model scaling see Tab. 2).

### 3.3.3 Experimental procedure and model development

Lateral compression was applied to the model at a rate of 2 cm/h up to 25, 37, 45 and 50% of finite shortening in eight simulations. Laboratory temperature was stable at around 19-20 °C during each experiment. The topographic images were captured every 10 minutes and saved in RAW (NEF) and JPG format (Digital SLR Camera Nikon D3200, 24.2MP, AF-S 18-55mm). The experiments show a similar evolution for all of the eight simulations with dominant deformation features that were

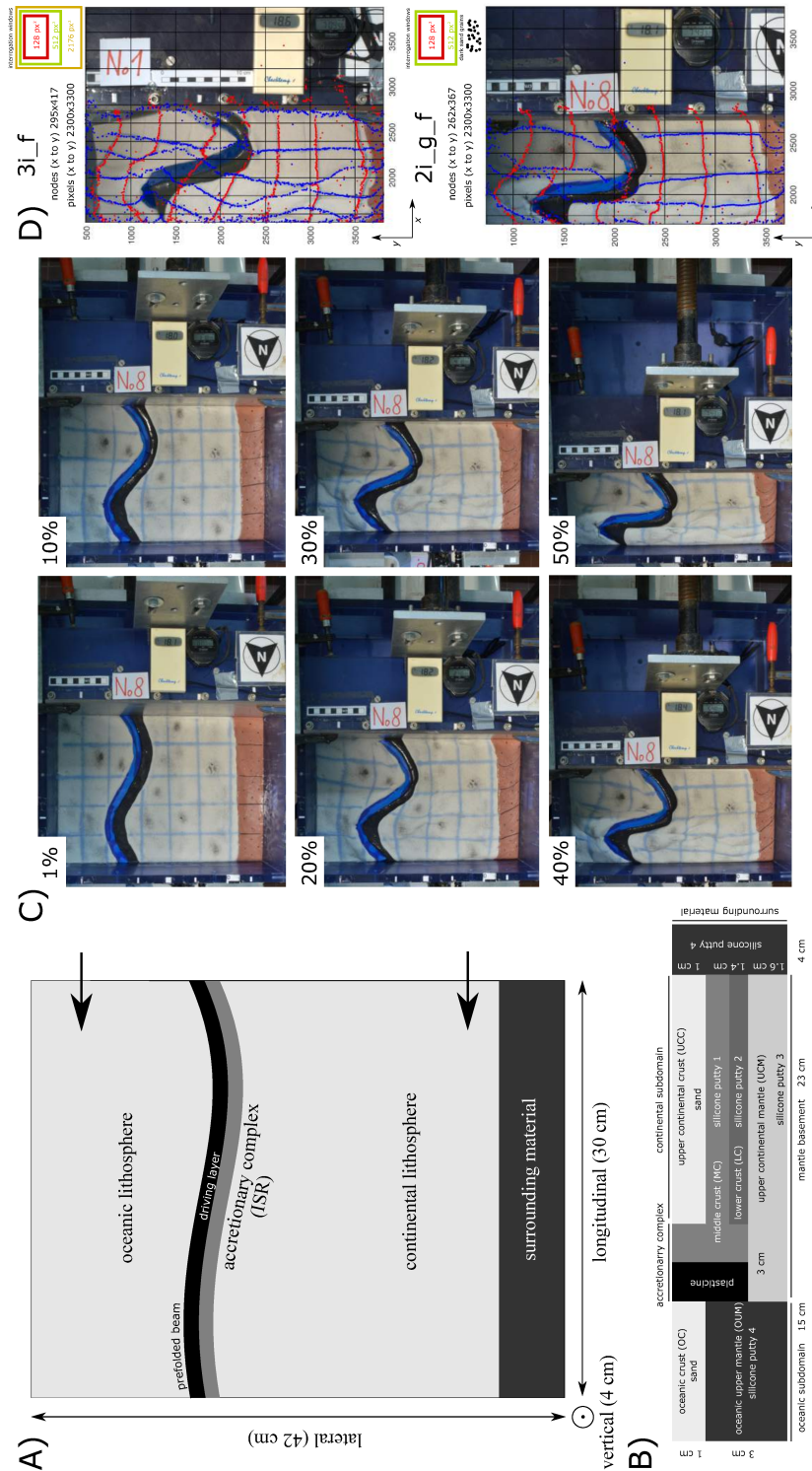


Fig. 24: Setup of the oroclinal buckling analogue model in plan-view (a) and lateral cross-section (b). Progressive evolution of the model domain during the lateral shortening is shown in (c). Qualitative test results of the displacement field obtained from the PIV (d,e), of variable image resolution, size of interrogation windows and type of PIV calculation. Red-blue grid is composed by individual markers that are transported by computed displacement in each time-step. Finite marker positions reflect well the finite deformation pattern. (d) 3i\_f represents three interrogation windows and image filtering, while (e) 2i\_g\_f represents two interrogation windows, additional dark particles dispersed on the surface and image filtering.

initiated already between 7-10% of shortening. These features are manifested by 1) amplification of the orocline with hinges that buttress into both adjacent lithospheric domains, 2) build up of upper crustal topographic perturbations manifested by the development of pop-up structures confined by thrusts with strike-slip components, and 3) rotation of the central model domain parts around the inflection point of the orocline.

### 3.3.4 Application of the PIV method for oroclinal buckling models

For the PIV analysis of all eight simulations, we used the MATLAB freeware toolbox PIVlab (Thielicke and Stamhuis, 2014). The method was used for model domains with identical initial geometry. For the last three simulations, the model surface was powdered by dark-coloured grains of sand, to enhance the PIV accuracy. The PIV analysis was performed on the surface of the model domain and excluded the masked surrounding image parts. We analysed 47 TIFF (uncompressed, 24-bit(true color, RGB)) images for each experiment with finite shortening of 50% in pairs (i.e. sequence 1-2, 2-3, 3-4...). The resolution of all the images is  $6016 \times 4000$  px (vertical to horizontal) where the analyzed domain represents  $7590000$  px<sup>2</sup>. We employed three interrogation windows ( $2176$  px<sup>2</sup>,  $512$  px<sup>2</sup>,  $128$  px<sup>2</sup>) in PIVlab and allowed additional pre-processing features as intensity highpass or CLAHE (contrast-limited adaptive histogram equalization) (Thielicke and Stamhuis, 2014, Raffel et al., 2007). For data post-processing, we used a validation module implemented in PIVlab to reject irrelevant (distant/false) values of the displacement field according to normalized median test (Nogueira et al., 1997; Westerweel and Scarano, 2005). Missing data were interpolated by the  $3 \times 3$  neighbourhood ( $3 \times 3$  mean) interpolation method (Nogueira et al., 1997; Thielicke and Stamhuis 2014; Boutelier, 2016).

The PIV procedure for our models comprised several post-processing algorithms. At first, we tested the accuracy of the calculated displacement field with respect to the different settings of the PIV calculations, input image formats and implementation of colour particles as physical markers (for increasing the PIVlab capability in recognizing the particle patterns in the image). The aim of the PIV tests was to achieve the best compromise between the resolution and accuracy of the resulting displacement field, evaluated by visual comparison of the real and calculated displacement. While the real displacement is defined by the movement of physical markers (an orthogonal grid of coloured sand lines or contrasting particles), the calculated displacement corresponds to the movement of virtual markers that match the original  $x, y$  positions of the pre-selected physical markers.

The testing procedure consists of the following steps: 1. Attribution of virtual point markers to initial physical markers (the finite position of physical markers that represent a surface sand grid) 2. application of a displacement to the virtual markers, 3. 2D interpolation of the displacement in new positions of the virtual markers from the surrounding nodal values (the calculated displacement grid is sparser than the

true displacement) for all time steps, and 4. imaging of the finite positions of virtual markers and their visual correlation with the position of physical markers. For all the tests, we scripted the associated procedures in MATLAB<sup>TM</sup> environment. Based on the best PIV settings, for further analysis of the model, we first chose the dataset calculated with additional filtering and a triplet of interrogation windows. This setting regards models where the surface resolution of the model was not enhanced by distributed dark particles (coloured sand grains). The accuracy test for this setting revealed only several local deviations from real material displacement (Fig. 24d). In the second approach, two interrogation windows were used in experiments (Fig. 24e), where the sand layer was covered by distributed dark particles (coloured sand grains) to increase the PIV accuracy. The resultant accuracy in the displacement field is comparable for both approaches.

### 3.3.5 Derived model parameters

Several velocity and strain-related parameters were derived from the calculated displacement field (Fig. 25). The first parameter represents the normalized magnitude of the velocity field. The next three parameters are the divergence of the velocity field, shear strain rate (second invariant of the deviatoric part of the strain rate tensor) and vorticity.

First, the strain-rate tensor (Eq. 3.1) and its deviatoric part (Eq. 3.2) was derived from the displacement between each of the model points (represented by the discrete numerical grid). The elements of the main diagonal of the tensor represent the stretches that are associated with the  $x, y$  directions, while the elements of the anti-diagonal correspond to distortion (for the symmetric part of the tensor (Eq. 3.3a)) or rotation (for the antisymmetric part of tensor (Eq. 3.3b)). The divergence of the velocity field (Eq. 3.4), is represented by the sum of elements situated along the main diagonal of the strain-rate tensor. Shear deformation is defined as the second invariant of the deviatoric strain-rate tensor (e.g. Becker and Kaus, 2015; Gerya, 2009) that shows the magnitude of isovolumic deformation, independently to the reference frame of the model (Eq. 3.5). The tendency of the material to rotate is expressed by the vorticity (Eq. 3.6).

$$\dot{\epsilon} = \frac{1}{2} \left( \nabla \cdot \vec{v} + \nabla^T \cdot \vec{v} \right), \quad (3.1)$$

$$\dot{\epsilon} = \begin{bmatrix} \epsilon_{xx} - \frac{1}{2}I_1 & \epsilon_{xy} \\ \epsilon_{yx} & \epsilon_{yy} - \frac{1}{2}I_1 \end{bmatrix}, \quad (3.2)$$

$$\dot{\epsilon}_{\text{sym.}} = \begin{bmatrix} \frac{\partial v_x}{\partial x} & \frac{1}{2} \left( \frac{\partial v_x}{\partial y} + \frac{\partial v_y}{\partial x} \right) \\ \frac{1}{2} \left( \frac{\partial v_y}{\partial x} + \frac{\partial v_x}{\partial y} \right) & \frac{\partial v_y}{\partial y} \end{bmatrix}, \quad (3.3a)$$

$$\dot{\epsilon}_{\text{antisym.}} = \begin{bmatrix} \frac{\partial v_x}{\partial x} & \frac{1}{2} \left( \frac{\partial v_x}{\partial y} - \frac{\partial v_y}{\partial x} \right) \\ \frac{1}{2} \left( \frac{\partial v_y}{\partial x} - \frac{\partial v_x}{\partial y} \right) & \frac{\partial v_y}{\partial y} \end{bmatrix}, \quad (3.3b)$$

$$\nabla \cdot \vec{v} = \dot{\epsilon}_{I_1} = \left( \frac{\partial v_x}{\partial x} + \frac{\partial v_y}{\partial y} \right), \quad (3.4)$$

$$\dot{\epsilon}_{I_2} = \varepsilon_{xx}\varepsilon_{yy} - (\varepsilon_{xy})^2, \quad (3.5)$$

$$\nabla \times \vec{v} = \left( \frac{\partial v_x}{\partial y} - \frac{\partial v_y}{\partial x} \right). \quad (3.6)$$

### 3.3.6 Correlation of the calculated parameters with deformation features

All calculated model parameters (magnitude of the velocity field, the divergence of the velocity field, shear strain and vorticity) were plotted for the three distinct stages of oroclinal buckling model evolution (Fig. 25) up to 20% of domain shortening. This initial deformation revealed a comprehensive correlation between the space-time changes of the strain-related parameters and the deformation features.

At first, we analyzed the velocity field which provides the first insight into the model dynamics (Fig. 25Aa-c) (All features that are described below are marked in the figure 25A by stars with corresponding numbering in the text). Here, the initial velocity increase reveals rapid amplification of the oroclinal hinge sector closer to the indenter side (1). The velocity field map reveals a curved frontline velocity gradient (Fig. 25Ab,c) (2) that is typical for arcuated deformation patterns in the indentation tectonics (Regard et al., 2005; Reiter et al., 2011) and accretionary wedge models confined between solid walls reflecting the Poiseuille type of flow (e.g. Grujic, 2006) (Fig. 25B). The zones of sharp velocity gradients are also related to the major deformation structures in the model that are also reflected by sharp space variations in other calculated parameters.

Negative anomalies in the divergence of the velocity field correspond to the thrust zones associated with the lateral propagation of the oroclinal hinges (Fig. 25e,f, (3)), thrusting (4) or underthrusting (5) outside of the oroclinal subdomains or pop-down structures (6) in the upper crust (Fig. 25f (6)). In contrast, positive values of divergence are related to areas of extension in crestal parts of upright folds, collapsing thrust belts or pop-up structures (7).

The contour diagram of shear strain (Fig. 25g,h,i) highlights two types of structures. First, the maximum values of shear rate reveals strong mechanical

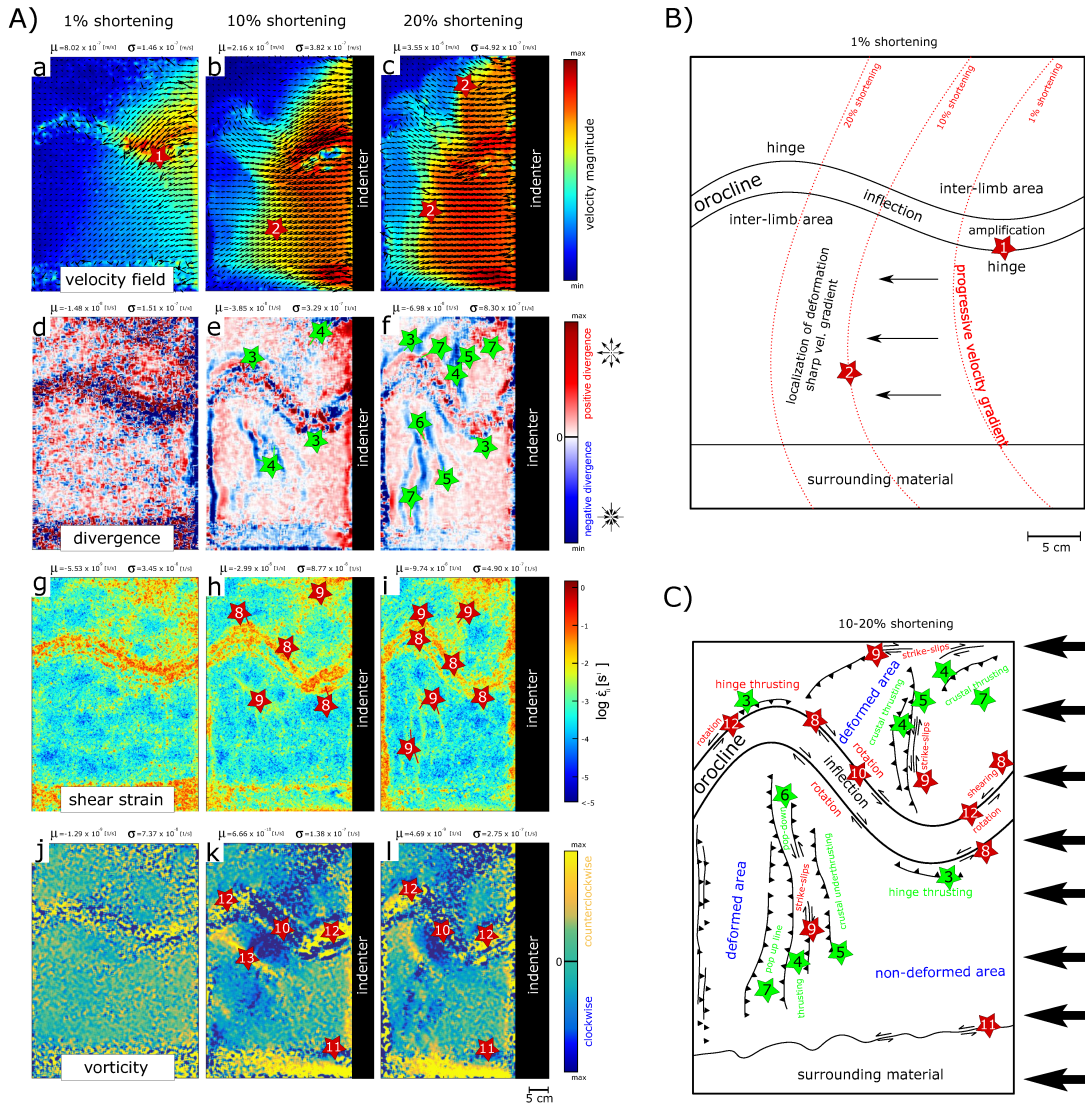


Fig. 25: Colour maps of PIV-derived parameters from the displacement field plotted for three distinct shortening stages (1%, 10% and 20%). From top to bottom (A), the parameters are: magnitude of displacement velocity with arrows representing vectors of displacement (a-c), divergence of velocity field (d-f), the second invariant of strain-rate tensor, equivalent to material shear strain-rate (g-i) and vorticity (j-l). All parameters except the strain-invariant are standardized (to obtain normalized z-scores for further analysis and to compare data from various experiments). Original average values and standard deviations are displayed in the small box above the current colour map. Panel (B) shows schematically the major features in the model domain as described in the text. Red lines show the progressive movement of the highest velocity gradient in time. Panel (C) represents a map of main deformation structures that are correlated with the variation of individual parameters displayed in panel (A). The red stars in the contour maps correspond with the deformation features that are described in the text and shown in panel (C).

decoupling along the rheological transition between the orocline and the surrounding subdomains (8). Second, elevated values of this parameter also correspond to strike-slip components of the thrusts and normal faults (9).

The restored vorticity field (Fig. 25j,k,l) reveals the clockwise movement of material elements around the inflection point sector of the orocline (10). This domain of clockwise rotation stretches in the direction parallel with the propagation direction of the orocline hinges. Another zone of relative clockwise rotation is situated in the lower right part of the model, in the confining silicone material adjacent to the brittle upper crustal domain (11). Counter-clockwise motion of the material is evident for the limbs on both ends of the orocline (12) and transitional zones (13) that divide subdomains of intense clockwise motion, dominated by rotational translation (orocline inflection) and regions, where deformation is dominated by volumetric distortion (pop-ups and pop-downs).

### 3.4 Models of detachment folding

#### 3.4.1 Model background and setup

The motivation for the detachment folding experiments was to understand the dynamics of folding in accretionary systems with a melt-softened lower crustal subdomain. Rheological stratification marked by a middle to lower crustal migmatitic layer is typical for many of the Phanerozoic orogenic belts at convergent plate boundaries (Vanderhaeghe et al., 1999, 2009). Late stage development of these orogens is associated with lateral and vertical bulk flow of the melt weakened, migmatitic domains, extruded from the core domains of the orogens e.g. in form of metamorphic core-complexes (e.g. Beaumont et al., 2001; Schulmann et al., 2008; Vanderhaeghe et al., 2009). The softening of lower crust in such systems is facilitated by e.g. slab-retreat driven pre-orogenic thinning in hot back-arc domains (Collins, 2002) and/or by emplacement of voluminous partially molten layer between the crust and upper mantle during a process known as “relamination” (Hacker et al., 2011; Lehmann et al., 2017; Maierová et al., 2018). The setup of the experiment (Fig. 26) was designed to mimic the development of a late Devonian accretionary belt, the Chandman metamorphic dome in the Central Asian Orogenic Belt, originally formed by a strong brittle upper crust (~15 km thick) and a weak partially molten layer (~15 km thick) in the lower crust above a strong granulitic residuum (Lehmann et al., 2017).

The crustal scale detachment folding experiments were performed using a narrow sandbox with a mobile heating plate (sheet metal with inner heating body) confined between the glass walls (Fig. 26A). Stable thermal gradients in superposed layers were attained by heat input from the heating plate and the light bulbs mounted on the top of thermally insulated apparatus. These gradients are marked by ~0.07 °C/mm and 0.06 °C/mm at the sides and the center of the model domain, respectively

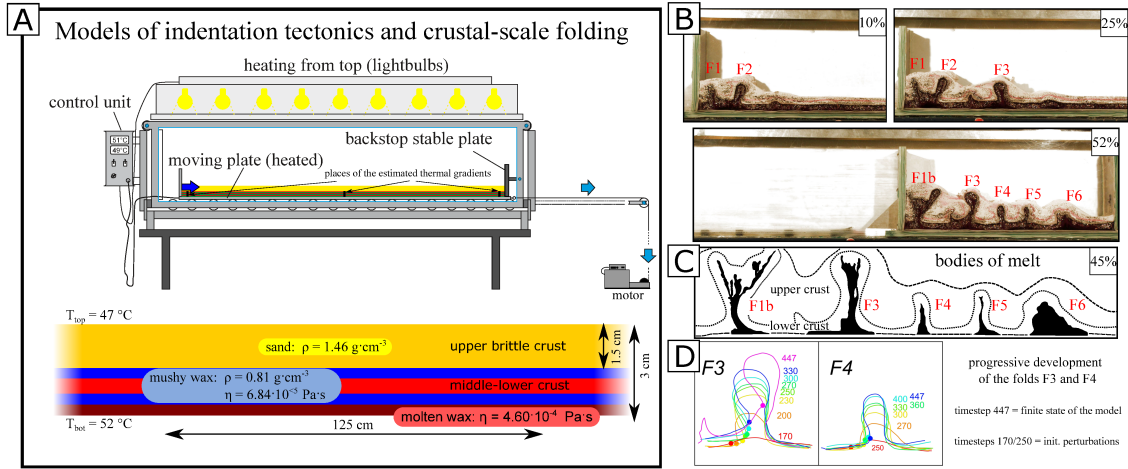


Fig. 26: Crustal scale detachment folding analogue model setup. Panel (A) shows experimental apparatus and model properties. Panel (B) represents progressive evolution of the model domain and sequential development of the folds for 10, 25 and 52% of shortening, respectively. Line drawing (C) highlights the boundaries between the different layers and the extent of redistributed wax melt in the fold cores (folds are marked F1b-F6, where F1b represents F1 and F2 that coalesced to the Y-shaped F1b fold). Progressive development of the folds F3 and F4 (D) show difference in body shape and mechanism of folding. Individual numbers represent timesteps where the actual shape was captured.

(Fig. 26, Tab. 3). During the experiments, the model domain on the mobile plate is pulled by a string reeled in by a motor at a constant rate against a stable vertical wall. The longitudinal, lateral and vertical dimensions of the model domain were 125 cm, 8 cm and 3 cm, respectively. The model consists of two layers, each 1.5 cm thick, the paraffin wax layer at the bottom and a fine-grained sand layer, representing the lower and upper crust, respectively.

The preliminary qualitative analysis of the resulting detachment folding experiments revealed that the amplification of the crustal scale detachment folds is associated with melt transfer from the bottom anatexic source to the core zones of growing folds. Therefore, in the following PIV quantitative analysis, we aimed to constrain the melt transfer dynamics between these subdomains. For related accuracy tests of the resulting displacement field after the post-processing (Fig. 28), we adopted the optimal PIV analysis setup, as applied for the oroclinal buckling models (Fig. 24D/24E).

### 3.4.2 Model materials and scaling

Paraffin wax *Paramo* with a melting point at 50 °C, manufactured by the *Paramo a.s.* Company in Czech Republic, was employed as the analogue of the thermally softened lower crust. The advantage of the paraffin wax is the thermally dependent rheology with Newtonian viscous properties in a molten state to slightly viscoplastic properties in a partially molten state below the melting point (Rossetti et al., 1999;

Tab. 3: Thermal profiles in the wax layer (see Fig. 26a for location of the profiles).

Depth (cm) / Temperature	left (°C)	central (°C)	right (°C)
T_surface	48,80	49,20	48,90
T_0.5	49,10	48,90	48,90
T_1.0	49,40	49,30	49,30
T_1.5	49,80	50,10	49,90
gradient (°C/mm)	0,07	0,06	0,07
gradient (°C/m)	66,67	60,00	66,67

\* profiles are shown in Fig. 4a

Tab. 4: Wax viscosities. Dynamic viscosities of the wax measured at the temperatures that characterize the viscosity gradient of paraffin wax in the crustal scale detachment fold experiment. Value marked with \* was obtained from the shear box experiments, value marked with \*\* was estimated according to shearing experiments and values published in Rossetti et al. (1999). The values for temperatures > 48 °C were obtained from rotational rheometer *VT 550 Haake* (Institute of Geophysics of the CAS, Prague).

Temperature (°C)	44*	46**	48	50	52
Viscosity (mPa.s)	1.01e9	1e5	0.85	0.53	0.46

Duarte et al., 2014). This range of rheological behaviour well corresponds to the rheological properties of anatectic lower crustal domains. The dynamic viscosities of the wax, that were measured by the *VT550 Haake viscometer* with coaxial cylinders (*MV1 cylinder*), range from 6.84 mPa.s at 44 °C to 0.46 mPa.s at 52 °C (Tab. 4).

The brittle upper crust in the models (1.5 cm thickness) is formed by pure quartz sand with an average size of 0.17 mm (quarried by *Sklopísek Střeleč co.*, Czech Republic). Ring shear test measurements revealed a friction coefficient of 0.7 and cohesion of 75 Pa (Klinkmüller et al., 2016; item 153-01 in the associated dataset). Before shortening of the model domain, a thermal and rheological gradient, marked by the low viscosity melt at the bottom and overlying visco(-elasto-)plastic partially molten wax, was attained after several hours of heating at the melting temperature of the wax (Fig. 26a). Before the experiment, the glass walls were sprayed with a low viscosity silicone to reduce the friction between the model domain and the glass walls.

The model was scaled according to the principles of geometric and dynamic-rheological similarity (Hubbert, 1937; Sokoutis et al., 2005). The geometric similarity is described by the scaling ratio  $l^* = 2 \cdot 10^{-6}$  with respect to the 30 km original crustal thickness prior to the accretion and folding (e.g. in the Chandman dome area, Lehmann et al., 2017). The accuracy of the dynamic scaling was tested by calculating the non-dimensional numbers defined by the ratios between the forces acting on the models. For the ductile lower crustal layer, we calculated the Ramberg number (Eq.

3.7; see Eq. 1.10 - 1.13), representing the ratio between the gravitational and viscous forces (**R<sub>m</sub>**; Weijermars and Schmeling, 1986; Sokoutis et al., 2005) as presented by Lehmann et al., (2017):

$$R_m = \frac{\text{gravitational stress}}{\text{viscous stress}} = \frac{\rho_d g h_d}{\eta \dot{\epsilon}} = \frac{\rho_d g h_d^2}{\eta V}, \quad (3.7)$$

where the  $\rho_d$  and  $h_d$  are the density and thickness of the ductile layer (paraffin wax), respectively,  $g$  is the gravity acceleration ( $g = 9.81 \text{ m} \cdot \text{s}^{-2}$ ),  $\eta$  is the viscosity of the ductile layer and  $\dot{\epsilon}$  the strain rate given by the ratio between the mean velocity of convergence  $V$  and the thickness of the ductile layer  $h_d$ .

Scaling of the brittle deformation in the upper crustal layer formed by the sand in the experiments was achieved by calculating the ratio between the gravitational stress and cohesive strength (**R<sub>s</sub>**; Ramberg, 1981; Sokoutis et al., 2005):

$$R_s = \frac{\text{gravitational stress}}{\text{cohesive strength}} = \frac{\rho_b g h_b}{\tau_c}, \quad (3.8)$$

where  $\rho_b$  and  $h_b$  represent the density and thickness of the brittle layer, respectively,  $g$  is the gravity acceleration and  $\tau_c$  the cohesive strength of the brittle layer. For correctly dynamically scaled model, the  $R_m$  and  $R_s$  calculated for both the model and the original (e.g. the Chandman dome; Lehmann et al., 2017), respectively, should be similar (Tab. 5).

The scaling analysis (Tab. 5) compares the viscosities of the partially crystallized wax measured at 44 °C (6.84 mPa.s, Tab. 3) and a migmatite, for which the viscosity is indirectly estimated from the viscosity of a suspension of a hydrous granite (hydrous rhyolitic melt containing ~ 1.5 wt.% water, Giordano et al., 2009) of ~ 108 Pa.s and 60-80 vol.% of crystals that increases the effective viscosity of the crystal/free melt 6-7 orders of magnitude to maximum ~ 1015 Pa.s (Costa et al, 2009). This scaling analysis (Tab. 5) shows similar values of both the  $R_m$  and  $R_s$  values for the experiment and the original, respectively. Alternatively, for the dynamic scaling analysis of the ductile layer, we can consider the viscosity of the completely molten wax (0.46 mPa.s at 52°C) as an equivalent to the same granite melt of ~ 108 Pa.s, but with 40-50% crystals that will render effective viscosity of the melt+crystal suspension of ~ 1013 Pa.s (Giordano et al., 2004, 2008; Costa et al., 2009). Calculating the corresponding  $R_m$  and  $R_s$  for both model and original will give again values within the same order of magnitude.

In summary, we can suggest that the rheological stratification of the sand and the wax quite well corresponds to the rheological stratification in thermally softened accretionary orogens, where the lower crust is formed by migmatites. The partially molten wax successfully implements a viscosity gradient from the completely molten

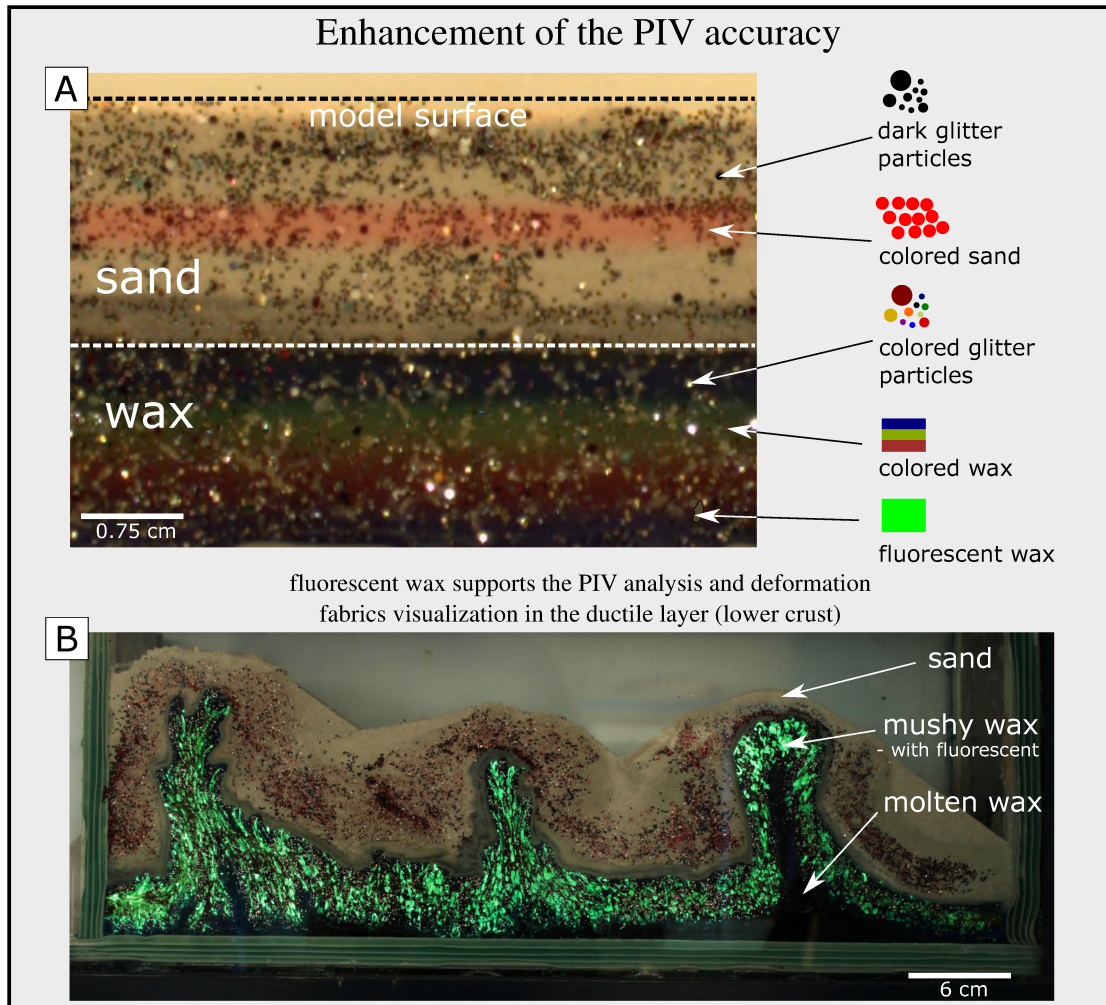


Fig. 27: Incorporated glitter particles in the sand and wax layers and additional shavings of fluorescent wax markers in the wax layer are shown in (a). Glowing markers of stretched fluorescent wax shavings in deformed model domain are shown in (b) (image was taken in dark room with long exposition). The black particles were incorporated into the sand layer while colour particles were superposed on the side wall of the wax layer. The setup of the illustrated model (b) represents the same physical properties of the analogue materials (i.e. sand, paraffin wax, fluorescent paraffin wax) as for the model described in Fig. 4, but with higher initial thickness of the model domain (3 cm sand layer, 3 cm wax layer) and shorter initial length (100 cm) than the model presented in Fig. 26 (120 cm). The 50% shortening of this model resulted in formation of three sequential detachment folds. The particles of the fluorescent wax highlight the finite deformation pattern in the mushy wax layer and are absent in the molten wax.

Tab. 5: Scaling analysis for the crustal scale detachment fold experiment.

parameters and units	Upper crust (sand in the experiment)				Lower crust (wax in the experiment)			g (m·s <sup>-2</sup> )	V (m·s <sup>-1</sup> )	R <sub>m</sub>	R <sub>c</sub>
	ρ <sub>b</sub> (kg·m <sup>-3</sup> )	h <sub>b</sub> (m)	f <sub>c</sub>	C (Pa)	ρ <sub>a</sub> (kg·m <sup>-3</sup> )	h <sub>a</sub> (m)	η <sub>a</sub> (Pa·s)				
model *	1460	0.015	0.63	156	810	0.015	8.5·10 <sup>-4</sup>	9.81	1.78·10 <sup>-4</sup>	11972360	3
nature *	2650	1.5·10 <sup>4</sup>	0.6	5·10 <sup>7</sup>	2750	1.5·10 <sup>4</sup>	1·10 <sup>15</sup>	9.81	6.34·10 <sup>-10</sup>	9571077	8

\* granitic melt with 1.5 wt.% water + 60-80 vol.% crystals; viscosity (melt+crystal) of 1·10<sup>15</sup> Pa·s

\* mushy wax (48 °C)

layer at the bottom of the lower crust to a partially molten layer close to the interface between the weak lower crust and a brittle upper crust.

### 3.4.3 Experimental procedure and model development

After attainment of the stable thermal gradient across the wax-sand multilayer, 55-60% shortening of the model domain was provided by the motion of the mobile plate against a stable backstop at the constant velocity of 1.3 cm/h (Fig. 26). Front side images were captured every 10 seconds by a single camera (*Canon EOS 1300D, 18Mpx, lens Canon EF-S 18-55mm f3.5-5.6 IS II*) mounted on a tripod. Images were saved in both the JPG format and RAW (CR2), later converted to TIFF (uncompressed, 24-bit(true colour, RGB)). Two point light sources were used to suppress the shadows in the background of the model domain. To decrease the reflexivity of the model glass walls, a whiteboard was mounted in the back wall of the apparatus.

A sequence of experiments performed at similar settings exhibits comparable trends in the evolution of the model domain marked by the development of up to five folds that developed sequentially during increasing shortening (Fig. 26b,c, folds F1b-F6). During the first 3-5% of shortening of the model displayed in Fig. 26, the model domain reflects homogeneous thickening followed by amplification of the first two folds (Fig. 26b, 10% of shortening). These first two folds later merge into one large Y shaped fold during the subsequent amplification of the remaining set of folds (Fig. 26b). All folds are associated with melt inflow into their hinge zones along the axial planes (Fig. 26c). Such melt inflow is manifested for example by axial plane-parallel finger-shaped channels in the core zone of complex fold F1b (Fig. 26b, c) that formed by coalescence of the first two folds F1 and F2. Long-lasting evolution of fold F3 was coupled with strong attenuation of the vertical limbs. The vertical limbs were at a late-stage of the evolution of the fold pinched by the surrounding sand as the left limb and the associated inflection point of the fold were progressively uplifted during progressive shortening of the model domain (Fig. 26d). This evolution was associated with isolation of paraffin melt in the diapirically shaped upper part of the fold above the pinched zone. A relatively large amount of melt was trapped also in the triangular zone below the pinched zone and above the source layer of paraffin melt (Fig. 26d). In contrast, the two following folds, F4 and F5, are marked

by lower height than the folds F1b and F3, homogeneously attenuated fold limbs and a relatively small amount of captured melt (Fig. 26d). Finally, the last fold in the sequence (F6, Fig. 26b) is marked by the highest proportion of melt that accumulated in the asymmetrical triangular zone below the crestal part of the fold.

#### 3.4.4 Improvement of colour variability for PIV analysis

Passive marker layers were incorporated in both, the wax and sand layers, to increase the visual resolution of the deformation features in the models. While the wax subdomain consists of a multilayer of five 0.3 mm thick layers of contrasting colour, only one stripe of red colour was included in the sand layer (Fig. 27b).

To enhance the PIV method resolution, we incorporated solid and circular passive markers that were randomly distributed on the front side of the model. These variably coloured markers are represented by small and flat glitter particles (Fig. 27a) of 0.1 - 0.5 mm in diameter. For the sand layer, we used the black colour dominated markers, while the more colourful glitter mixtures were superposed on the wax layer.

To visualize the finite deformation pattern, we tested the applicability of fluorescent wax shavings (Fig. 27a) that were again sprinkled on the frontal side of the wax layer. These variably shaped and elongated particles served as passive markers that were deformed during the domain shortening and were aligned and stretched parallel with the axial planes of the developing folds. The finite deformation pattern as visualized by these particles was then photographed with a long time exposure in darkness (Fig. 27c).

#### 3.4.5 The PIV calculations and testing of accuracy

The displacement field was calculated from all the sequential pairs of 445 analyzed images (TIFF format). The images, with a resolution of  $5202 \times 3465$  px (horizontal  $\times$  vertical), were cropped by a mask, defining the model domain. The PIV calculations were performed with the setting corresponding to the PIV analysis of the oroclinal buckling models. We used three interrogation windows ( $2176 \text{ px}^2$ ,  $512 \text{ px}^2$ ,  $128 \text{ px}^2$ ) for subareas of the images ( $4801680 \text{ px}^2$  at an initial non-contracted state where the deformable model domain is represented by  $885312 \text{ px}^2$ ) representing the deformed model domain. Image pre-processing (additional image filtering and contrast enhancement) were done using the PIVlab interface (see chapter 3.3.4 or 3.8.3). The resulting displacement field contains  $319 \times 57$  (horizontal to vertical) node points.

As in the oroclinal buckling models, we tested the accuracy of the PIV post-processing using the virtual markers. The virtual markers were positioned along the horizontal line following the red stripe in the sand layer and one of the layers in the wax multilayer (Fig. 28). Application of the integrated displacement for each marker and for all the time steps resulted in a very good match with the finite state

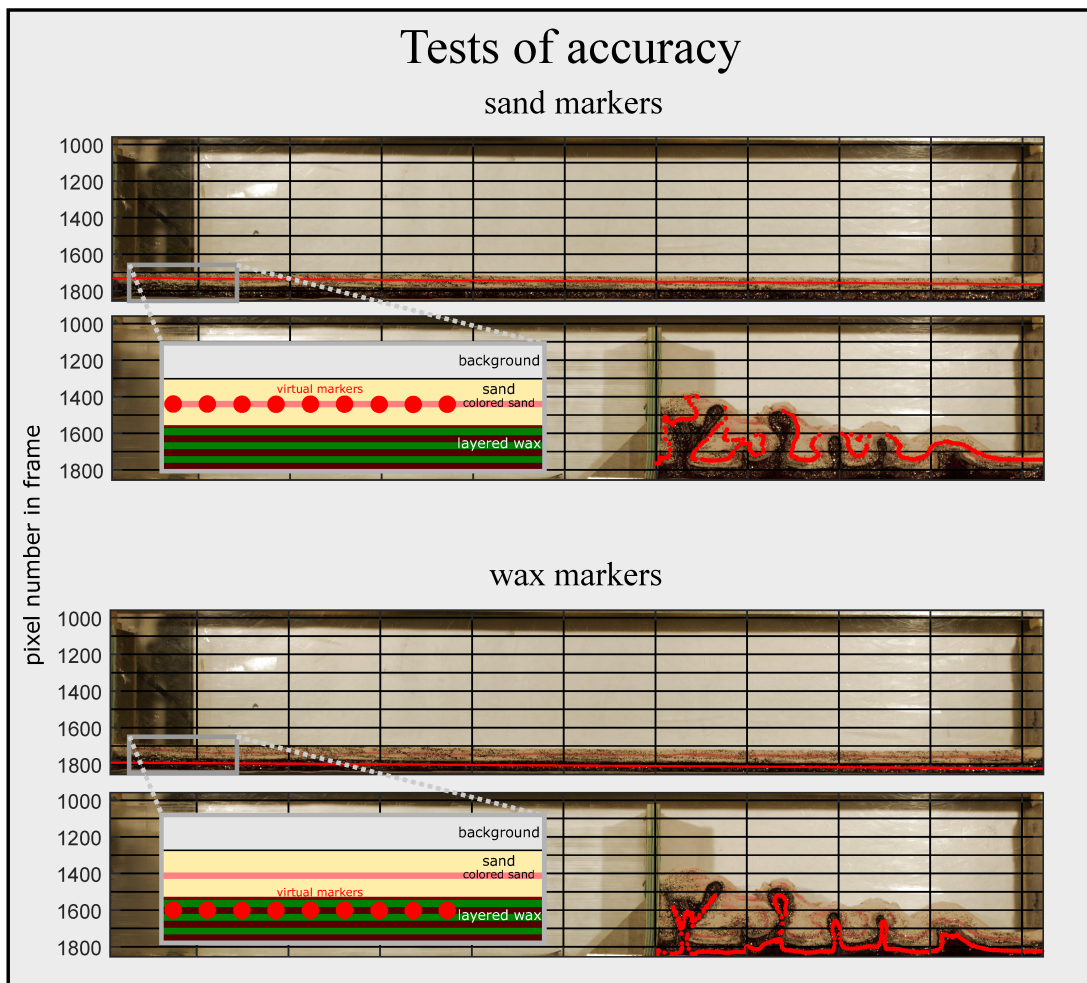


Fig. 28: Qualitative test results of the PIV for laboratory simulations of detachment folding. Top two figures show initial and final position of the markers distributed along the red line in the sand layer. Bottom two figures show a similar match for the initial and finite position of equivalent markers situated in the wax layer.

pattern of the experiment. The positions of the virtual markers trace the folded passive markers and displacement around the thrusts in the sand layer (Fig. 27b, 28). This test suggests that the calculated displacement field reliably reflects the final deformation pattern.

### 3.4.6 Derived model parameters

The contour maps of the strain-related parameters derived from the displacement field were analyzed only for the first 30% shortening since the evolution of the associated fields shows recurrent patterns during the sequential folding (Fig. 29). All the displacement field features that are described in the text below are marked by stars with corresponding numbering in figure 29A. The velocity displacement field map reveals a sharp gradient along the longitudinal direction that corresponds to the amplification of lastly developing fold (Fig. 29A-a (1)). From the ~10% of shortening, the velocity gradient becomes more gradual.

The positive and negative divergence of the velocity field represents primarily the locations of extension and compression in the model domain, respectively. In the sand layer, the positive anomalies correspond to the extensional crestal part of the folds (Fig. 29A (2)), while the negative values match with the compressional, synclinal sectors located between the individual folds (3) and at the interface of the wax and sand above the initial fold perturbations (4). Aerially extensive domains of negative divergence in the foreland flanking fold limbs in the sand are associated with the motion of the model domain with respect to the immobile background (5). Therefore, these anomalies can be regarded as artefacts of the experimental setup and cannot be interpreted in terms of the inner deformation dynamics. Finally, pairs of close spatially associated negative and positive anomalies are situated in the triangular domains at the base of the developing detachment folds (6). These sites correspond to the visual inflow of melt from the source layer to the axial and crestal parts of the developing folds. While the left sides of these triangular zones are coupled with negative divergence, the right sides of these triangles show positive divergence values.

The second invariant of the strain-rate tensor (isovolumic strain-rate) reveals maximum shear rates at the surface of the model domain (7). This pattern is again linked to the movement of the model domain in front of the immobile background, similar to the negative divergence on the right side flanking slopes above the folds. In the interior of the model domain, high shear rates are linked with locations of fore- and back-thrusts in the sand (8) and axial planes of folds in the wax (9). The last significant localization of shear is associated with the triangular zones at the bottom of the melt-cored detachment folds (10).

In the vorticity field (Fig. 29A,j-l), we observe counterclockwise rotational movement at the model surface (11), which is again associated with the relative movement of the model domain with respect to the stable model background. In the



inner part of the model domain, the vorticity anomalies correspond to the clockwise and anti-clockwise motion related to the fore-thrusts (12) and back-thrusts (13), respectively.

### 3.5 Divergence and the volumetric flow on local scale in the detachment fold experiments

The divergence parameter in the detachment fold experiments was employed for tracing the volumetric changes derived from the velocity field that were analyzed from the cross-section of the accretionary system (side-view) (Fig. 26, 29). This approach is analogous to the oroclinal buckling models (Fig. 24, 25), where the divergence parameter was employed on plan-view image datasets for dynamics of topography evolution. The motivation for the detailed divergence analysis in the detachment fold experiments was a deeper understanding of the deformation and relative material transfers in the selected parts of the models.

In particular, we wanted to quantify the flow dynamics of melt and surrounding partially molten wax during the progressive development of the detachment folds, because the final fold shapes are apparently linked with the relative amount of melt available in the source layer (true amount of the melt transferred from the close surroundings of the amplifying folds) and the rate of vertical melt injection along the axial plane of the folds. Detailed inspection of the upward melt flow zones revealed that the melt is transferred in a coherent single channel (e.g. fold F3, Fig. 26; Fig. 27c) or through several discrete and narrow, finger-shaped channels surrounded by the mushy wax (e.g. fold F1b, Fig. 26). Since the geometry of the folds and the flow channels are clearly different across the studied sequence of the detachment folds in a single experiment, we decided to trace the variations of the divergence parameter in time and space.

At first, we focus on small-scale details of the models and analyze the displacement field in a predefined static image window. This window is fixed with respect to the background of the moving material in the model (Fig. 30) and locked at the original level of the mushy wax zone, where discrete melt channels develop at later stages of the model evolution (e.g. in fold F1b, Fig. 26, 29c). In the second approach, we develop the mobile and adaptive subgrids, fixed on pre-selected subdomains in the model domain (e.g. fixed on the axial plane of a specific fold), where the divergence is calculated.

#### 3.5.1 Divergence in a static window

In order to understand the deformation pattern related with melt transfer on a local scale, the window used for the PIV calculations was fixed at a position in the foreland of the first two developed folds in the mushy wax layer (timestep 100/450; Fig. 30a). We traced the deformation field in this small window until the time step

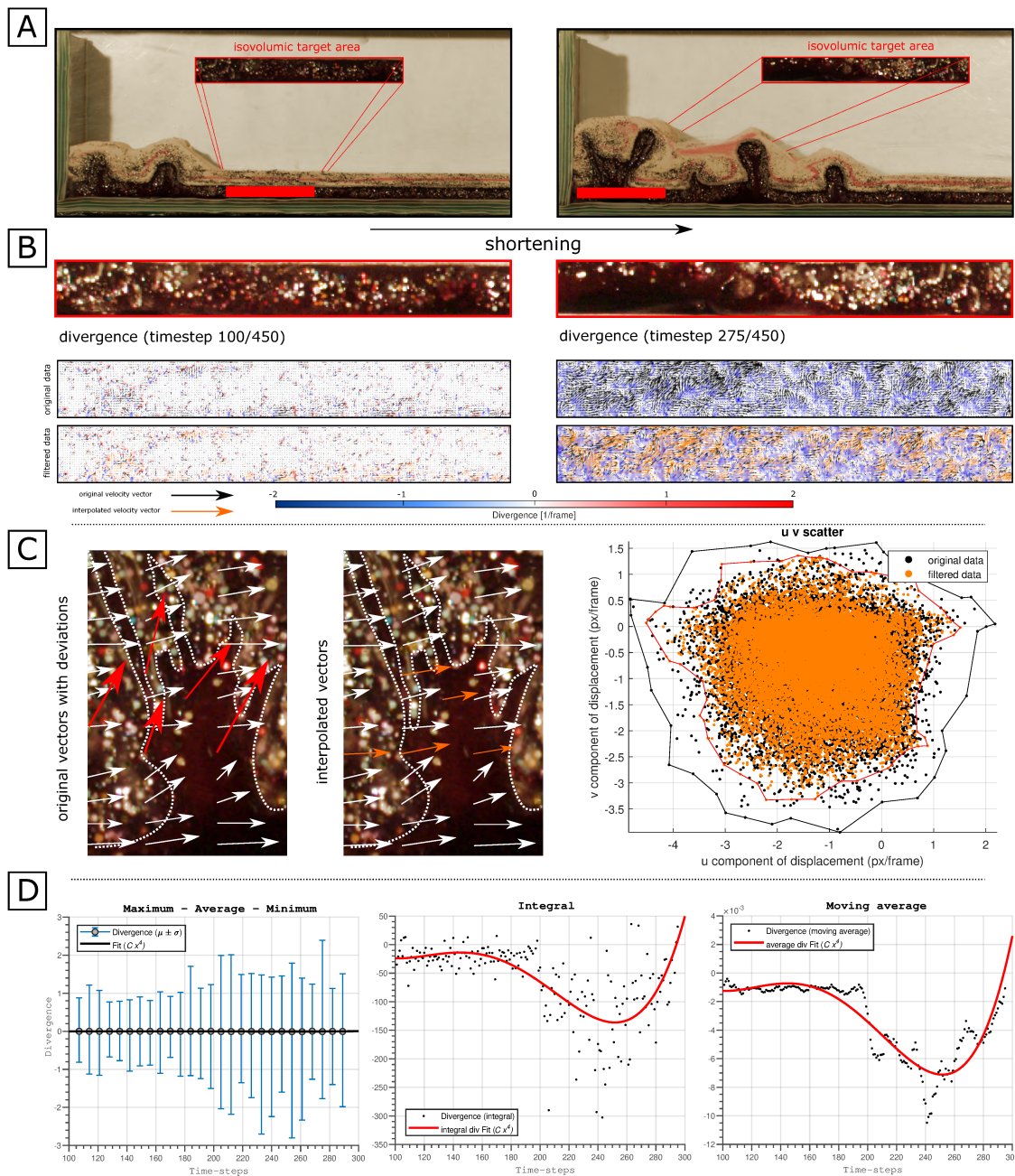


Fig. 30: Application of the divergence for investigation of volumetric flow. Panels A and B display the model domain in two distinct stages of the model evolution and a static window where the divergence of the velocity/displacement field was calculated. Panel B shows the displacement vectors and divergence field in the static window for corresponding time-steps, before and after filtering of the velocity field by substitution of vector deviations from the velocity background (filtration scheme follows the  $3 \times 3$  median test: e.g. Nogueira et al., 1997; Westerweel and Scarano, 2005). The substitution of rejected vectors by 2D interpolation (c), includes scatterplot of u,v components of the velocity field before and after filtration. Red arrows represent the original displacement which is locally substituted by new interpolated values (yellow arrows). Diagrams of time-evolution of the divergence in static window shown in (D) were calculated from filtered displacement field (maximum - average - minimum divergence, integral divergence, moving average).

300/450, (Fig. 30a,b), when the core zone of fold F1b completely overlapped with this window during progressive shortening. At first, we calculated the divergence from the original displacement field obtained from the PIV with settings described in section 3.4.5. In the following calculations, we reshaped the interrogation windows in the PIV settings for the image subsamples corresponding to the dimensions of the static window (to 512 px<sup>2</sup>, 128 px<sup>2</sup>, 32 px<sup>2</sup>). The analyzed image window represents the area of 75336 px<sup>2</sup> cut from the original image of the model domain with a size of 885312 px<sup>2</sup>. The resultant vector field which is shown in Fig. 30b contains 49×391 nodes.

Preliminary analysis of the displacement field in the static window revealed velocity gradients on small scales (Fig. 30b) marked by e.g. anomalous vectors (Fig. 30c) that are associated with the melt flow through small finger-shaped channels in the lower parts of the model (Fig. 30c). This melt propagation and ascent into the cores of developing folds is apparently independent of the background displacement field which is related to the displacement of the whole model domain.

We realized that standard filtering procedures could significantly alter the distribution of divergence and interpretation of the local melt flow patterns. Therefore, we decided to intentionally attempt to filter all the anomalous vectors that are related with the small scale (finger shaped) channels transferring the melt from the source domain to the overlying folds (Fig. 30c). This procedure implements artificial distortions of the displacement field, where the anomalous vectors were replaced with interpolated values. As a result, the modified displacement field is characterized by non-zero values of integrated divergence that can be interpreted in terms of melt inflow, accumulation and outflow.

Figure 30d displays the local and areal divergence in the static isovolumic area (predefined static window) in time that corresponds to progressive folding of the model domain in front of, and later above, this area. The divergence values reveal a relatively small variation range for the first part of the studied image sequence (100-170/450) with average values close to zero (Fig. 30b,d). The difference between extreme values progressively increases with domain shortening from timestep 180. The integral values (areal divergence), as well as the average values of divergence (Fig. 30d), show a non-linear trend with decreasing values up to timesteps 240-260 followed by progressively increasing values up to a timestep 290.

This evolutionary trend may be attributed to an increasing melt transfer rate between the source area (basal layer) and the core of the growing fold (decreasing divergence). The minimum values are associated with a high rate of material inflow, resp. with an increasing amount of the melt which is distributed in the target area. As the amplification of the F1b fold is slowing down, the rate of the melt inflow decreases and the divergence increases back to zero values.